# Monte Carlo simulations of the capture and cooling of alkali-metal atoms by a supersonic helium jet

Jeremy Glick, William Huntington ⬤, Michael Borysow ⬤, Kevin Wen ⬤, and Daniel Heinzen ⬤
*Department of Physics, University of Texas at Austin, Austin, Texas 78712, USA*

Jacek Kłos and E. Tiesinga
*Joint Quantum Institute, National Institute of Standards and Technology and Department of Physics, University of Maryland, Gaithersburg, Maryland 20899, USA*

We present three-dimensional Monte Carlo simulations of the capture of 1000 K $^7$Li or 500 K $^{87}$Rb atoms by a continuous supersonic $^4$He jet and show that intense, cold alkali-metal beams form. The simulations use differential cross sections obtained from quantum scattering calculations of $^7$Li or $^{87}$Rb atoms with $^4$He atoms for relative collision energies between $k \times 1$ mK and $k \times 3000$ K, where $k$ is the Boltzmann constant. For collision energies higher than approximately $k \times 4$ K the collisions favor forward scattering, deflecting the $^7$Li or $^{87}$Rb atoms by no more than a few degrees. From the simulations, we find that about 1% of the lithium atoms are seeded into the $^4$He jet, resulting in a lithium beam with a most probable velocity of about 210 m/s and number densities on the order of $10^8$ cm$^{-3}$. Simulations predict narrow yet asymmetric velocity distributions which are verified by comparing to fluorescence measurements of the seeded $^7$Li atoms. We find agreement between simulated and experimentally measured seeded $^7$Li densities to be better than 50% across a range of $^4$He flow rates. We make predictions for seeding efficiency and cooling of $^{87}$Rb by a supersonic $^4$He jet. The seeding efficiency for $^{87}$Rb is expected to be similar to $^7$Li.

## I. INTRODUCTION

Seeded supersonic jets serve as a valuable tool for producing intense cold beams having long been used for studies in molecular physics, fluid dynamics, and molecular spectroscopy [1–5]. In these systems cooling is achieved via the adiabatic expansion of a carrier gas, typically a noble gas, from a nozzle. Historically, seeding of noncondensible atoms or molecules generally occurs by mixing into the carrier gas well in advance of the jet nozzle. Condensible species can be seeded just before or immediately after the nozzle; this arrangement is known as a Smalley source [5,6]. Temperatures of seeded supersonic jets have generally been on the order of 1 K [1,2,5,7,8], with some sources producing values as low as 0.2 K [9,10], where no further cooling is applied postexpansion [11]. Depending on the temperature of the jet's nozzle and carrier gas species, forward velocities are generally in excess of 500 m/s.

In Ref. [12], some of us described an alternative approach where seeding is performed postexpansion of the carrier gas. Utilizing highly expanded helium jets where submillikelvin temperatures can be achieved in the moving frame [13,14], a seeded beam of $^7$Li was produced with a temperature on the order of 10 mK and continuous peak intensity on the order of $10^{12}$ cm$^{-2}$ s$^{-1}$. By performing postnozzle seeding, the nozzle of the jet could be cooled to 4.2 K to greatly reduce the forward velocity of the beam to 210 m/s while also eliminating the heat load on the nozzle and condensation that may otherwise occur with a continuous lithium source and relatively small nozzle diameters. The combination of low temperature, relatively low forward velocity, and high inten-

sity makes atom-optical manipulation of the beam such as magnetic focusing highly effective [12]. Modeling the seeding process is crucial for optimizing the source's performance to enable the production of similarly intense cold beams of other species. Over the years, researchers have examined prenozzle seeded jets [15–17]; however, modeling of the postnozzle seeding of an effusive beam into a supersonic jet is lacking.

Determining conditions for efficient postnozzle seeding requires knowledge of the collisional properties between alkali-metal atoms and noble-gas atoms. Such properties have been extensively studied over the past 60 years. For example, the collision-energy dependence of the elastic-scattering cross sections for collisions between $^7$Li and noble-gas atoms were measured in the early 1970s [18,19]. Diffusion coefficients describing the propagation of density gradients of trace amounts of alkali-metal atoms in noble-gas buffer gases have been computed as well as measured [20–23]. Potential energy surfaces as well as rates coefficients have been computed as well [24–26]. The single bound state for the $^7$Li$^4$He system, for example, predicted in Ref. [27], was observed in Ref. [28]. Ultracold microkelvin and millikelvin samples of $^7$Li and $^{87}$Rb atoms are used to measure pressure in the ultrahigh vacuum (UHV) regime [29–36]. These devices rely on precise knowledge of thermalized elastic rate coefficients between the ultracold alkali-metal atoms and the ambient-temperature atomic and molecular gases in the UHV regime. To validate these devices, known pressures of ambient temperature background gases, often noble gases, are deliberately added into the vacuum chamber [37].

To model the seeding process, it is crucial to understand the velocity phase-space distribution of the carrier gas. Models
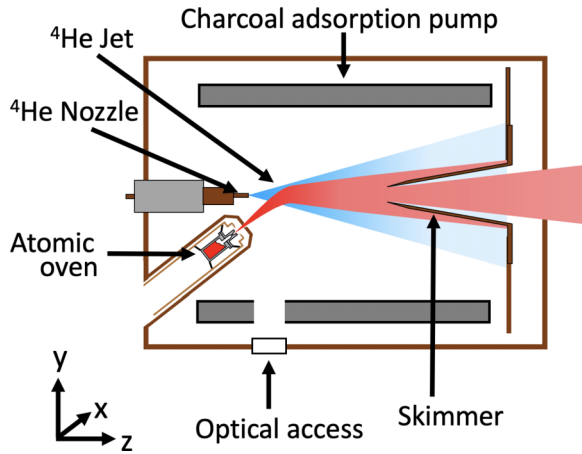
FIG. 1. Schematic of the apparatus showing lithium or rubidium atoms (red region) created in a hot atomic oven, captured by a supersonic cryogenic helium jet (cyan region), and then extracted with a skimmer. The lower left corner shows the Cartesian $xyz$ coordinate system used in the simulations. The $y$ and $z$ axes are in the plane of this image, while the origin is at the tip of the cryogenic $^4$He sonic nozzle. In the experimental realization, a charcoal adsorption pump is used to remove background helium. A camera collects fluorescence emitted in the $x$ direction that is induced by probe lasers directed vertically through the window labeled optical access or horizontally along the centerline of the helium jet.

of supersonic expansions have been performed using various numerical methods as a means of finding approximate solutions to the Boltzmann equation for the phase-space density of the atomic species and molecules. Early research utilized the method of moments approach [38–40] enabling studies of the decoupling of the transverse and longitudinal temperatures when the jet transitions from continuum or fluidlike flow to free molecular flow. Modern simulations are often performed using computational fluid dynamics (CFD) solvers [41,42] or direct-simulation Monte Carlo (DSMC) simulations [43–45]. Both CFD and DSMC can model turbulent flow and shock front formation as well as evaluate the role of nozzle geometry on beam brightness.

Here we report on three-dimensional (3D) Monte Carlo simulations of the capture of $^7$Li and $^{87}$Rb by a supersonic helium jet. We quantify the fraction of lithium and rubidium atoms that become entrained in the jet over a wide range of helium flow rates using accurate theoretical differential cross sections for $^7$Li-$^4$He and $^{87}$Rb-$^4$He scattering. Simulated density and velocity profiles are presented and analyzed. We compare data from $^7$Li experiments to validate our approach. Extensions of this work can be used to design similar post-nozzle seeded apparatuses for the production of intense cold beams of various species.

## II. EXPERIMENTAL SETUP AND THEORETICAL TREATMENT

We model the dynamics of seeding and cooling energetic $^7$Li or $^{87}$Rb atoms into a supersonic helium jet. A schematic of the simulated apparatus and the definition of our coordinate system are shown in Fig. 1. The helium sonic nozzle is

directed in the (0,0,1) or $\hat{z}$ direction with its tip located at the origin $\vec{x}_N = (0, 0, 0)$ of our coordinate system. The helium nozzle diameter $d_N = 0.020$ cm. Here and elsewhere system parameters are motivated by the designs of Ref. [12]. The alkali-metal source creating an effusive beam of atoms is oriented in the $(0, \sin \theta_S, \cos \theta_S)$ direction with angle $\theta_S = 50°$ from the $\hat{z}$ axis, where the opening or aperture in front of the oven is located at $\vec{x}_S = (0, -5.6, -3.0)$ cm. This source has a conical nozzle with an aperture diameter of $d_S = 0.10$ cm. The nozzle diameters are thus much smaller than $|\vec{x}_N - \vec{x}_S|$. Moreover, the geometrical intersect or seeding distance between the helium jet and alkali-metal beam directions is 1.7 cm downstream from the helium nozzle. A skimmer extracts the cold alkali-metal atoms. The skimmer is located 16 cm from the helium nozzle and has a circular opening with a diameter of 2.54 cm. The line connecting the nozzle and the opening of the skimmer defines the centerline of the helium jet.

The orientation and location of the alkali-metal source relative to the helium jet are by no means unique. For specificity, however, our simulations closely match the physical design constraints of the implementation in Ref. [12]. In principle, this restricts our ability to optimize the design. In practice, we find that optimizing the flow rate of the $^4$He jet is sufficient for creating intense cold-alkali-metal-atom beams.

### A. Static helium jet

The motion of all helium and alkali-metal atoms can in principle be modeled with the DSMC method. The efficient seeding of the alkali-metal (AM) atoms, however, requires a dense helium jet. Our expected stagnation helium number densities $n_0$ are a few times $10^{19}$ cm$^{-3}$ with a stagnation temperature of the helium atoms of about $T_0 = 4.2$ K. The stagnation conditions are the conditions in the reservoir before the nozzle. Based on these conditions, the mean free path between $^4$He-$^4$He collisions is a few microns using the $^4$He-$^4$He cross section from Ref. [46]. This puts the expansion well into the continuum regime where simulations using the DSMC method are challenging. Furthermore, we cannot take advantage of the 2D axial symmetry of the helium jet and a 3D simulation is required to model the injected alkali-metal-atom beam.

We therefore introduce approximations based on the realization that the number densities of the alkali-metal atoms is orders of magnitude smaller than those in the helium jet. First, the mean free path between AM-AM collisions is larger than the centimeter size of the system so only one alkali-metal atom needs to be followed at a time. Second, the value for the mean free path between AM-$^4$He collisions lies between those for $^4$He-$^4$He and AM-AM collisions. Then the number density of the $^4$He jet and the relationships among the mean free paths have several implications. The heat added to the helium jet as the alkali-metal atoms slow can be neglected. Consequently, we can assume that the helium jet is expanding adiabatically, is in the collisional regime, and is locally always in thermal equilibrium. In other words, we can treat the jet as a static background flow and only need to determine lithium trajectories as they collide with $^4$He atoms.

From Refs. [47,48] it can be shown that the unit-normalized position and velocity phase-space probability distribution of the axially symmetric expansion of the helium atoms in the jet starting from position a few nozzle diameters away is well described by

$$P_{\text{He}}(\vec{r}, \vec{v}) = c_0 \left( \frac{m_{\text{He}}}{2\pi k T_0} \right)^{3/2} \zeta(\hat{r}) \exp$$
$$\times \left( -\frac{1}{2} \frac{m_{\text{He}}(\vec{v} - v_{\text{He,tv}} \hat{r})^2}{k T_{\text{He}}(r)} \right), \quad (1)$$

where $\hat{r} = \vec{r}/r$ is the orientation of $\vec{r}$ in the Cartesian coordinate system defined in Fig. 1. In spherical coordinates $\hat{r}$ is specified by polar angle $\theta \in [0, \pi]$ and azimuthal angle $\varphi \in [0, 2\pi]$. In addition, the position-dependent helium temperature and radial terminal or streamline velocity are

$$T_{\text{He}}(r) = c_1 T_0 \left( \frac{d_N}{r} \right)^{4/3} \quad (2)$$

and

$$v_{\text{He,tv}} = \sqrt{5 \frac{k T_0}{m_{\text{He}}}}, \quad (3)$$

where $m_{\text{He}}$ is the mass of the $^4$He atom and $k$ is the Boltzmann constant. Here coefficients $c_0 = 1.62$ and $c_1 = 0.287$. Finally, the angular function $\zeta(\hat{r})$ is given by

$$\zeta_{\text{He}}(\hat{r}) = \frac{1}{\mathcal{Z}(t_{\text{He}})} \cos^2(t_{\text{He}}\theta) \quad (4)$$

for $0 \leqslant \theta < \pi/(2t_{\text{He}})$ and zero otherwise. We have $t_{\text{He}} > 1$ and $\mathcal{Z}(t_{\text{He}})$ is defined such that $\int_0^\pi \sin\theta \, d\theta \int_0^{2\pi} d\varphi \, \zeta_{\text{He}}(\hat{r}) = 1$. For a sonic nozzle and helium carrier gas, $t_{\text{He}} = 1.15$ and $\pi/(2t_{\text{He}}) = 78°$. Locally, after integrating $P_{\text{He}}(\vec{r}, \vec{v})$ over all velocities and using Eq. (2), we find that

$$p_{\text{He}}(\vec{r}) = \int d^3\vec{v} \, P_{\text{He}}(\vec{r}, \vec{v}) = c_0 c_1^{3/2} \left( \frac{d_N}{r} \right)^2 \zeta_{\text{He}}(\hat{r}) \quad (5)$$

and similarly that the root-mean-square velocity in the moving frame of the helium gas is

$$v_{\text{He,rms}}(\vec{r}) = \sqrt{3 \frac{k T_{\text{He}}(r)}{m_{\text{He}}}}. \quad (6)$$

The helium number density is

$$n_{\text{He}}(\vec{r}) = n_0 p_{\text{He}}(\vec{r}) = c_0 c_1^{3/2} n_0 \left( \frac{d_N}{r} \right)^2 \zeta_{\text{He}}(\hat{r}), \quad (7)$$

where

$$n_0 = 0.513 \sqrt{\frac{1}{2} \frac{m_{\text{He}}}{k T_0}} \left( \frac{4}{\pi d_N^2} \right) \dot{N}_0 \quad (8)$$

and $\dot{N}_0$ are the helium number density and number flow rate at the sonic nozzle, respectively [48]. Typical helium flow rates are between $2 \times 10^{19}$ and $1 \times 10^{20}$ s$^{-1}$ [12].

The phase-space distribution defined in Eqs. (1)–(4) breaks down for radii smaller than a few nozzle diameters, that is, the local helium temperature $T_{\text{He}}(r)$ should approach $T_0$ for small $r$. Equation (1) also breaks down for large radii $r$, where the

$^4$He-$^4$He collision rate is insufficient to maintain local thermal equilibrium resulting in different transverse $x$ and $y$ and longitudinal $z$ velocity distributions [38,49]. In the Appendix we discuss how modifications to the helium temperature affect the seeding efficiency.

In the experiments of Ref. [12] and in our simulations, $T_0 = 4.2$ K and the largest allowed radius $r$ for which Eq. (1) is expected to be valid is about 10 cm for the lowest helium reservoir densities which we consider. From Eq. (2) the initial helium temperature implies that the helium temperature drops to 7 mK approximately 1 cm away from the sonic nozzle. The terminal velocity for $^4$He atoms is approximately equal to 210 m/s. The terminal kinetic energy is $m_{\text{He}} v_{\text{He,tv}}^2/2 = 5kT_0/2 \approx k \times 11$ K. As a general feature of supersonic expansion, we realize that $v_{\text{He,tv}} \gg v_{\text{He,rms}}(r)$ for $r \gg d_N$.

### B. Collision cross sections

The Monte Carlo simulations rely on an accurate knowledge of the differential cross section

$$\frac{d\sigma_{\text{AM-He}}}{d\Omega} \quad (9)$$

for collisions of $^7$Li and $^{87}$Rb with $^4$He, each in its $^2S$ or $^1S$ electronic ground state, as a function of relative collision energy $E$ and polar and azimuthal collision angles $\theta_c$ and $\varphi_c$. We also use the total elastic cross section

$$\sigma_{\text{AM-He}}(E) = \int_0^\pi \sin\theta_c d\theta_c \int_0^{2\pi} d\varphi_c \frac{d\sigma_{\text{AM-He}}}{d\Omega}. \quad (10)$$

Formal discussions of scattering theory describing cross sections and collision angles but also partial waves, centrifugal barriers, and Wigner threshold laws can be found in Refs. [50–52].

We rely on the recent evaluations of the relevant $X\,^2\Sigma^+$ potential energy curves as functions of the interatomic separation $R$ defined as a distance between pointlike atomic nuclei and numerical solutions of the Schrödinger equation for the relative motion of the atoms using these isotropic potentials by some of us in Refs. [36,53,54]. An isotropic potential only depends on $R$ and not the orientation of the interatomic axis. We use the reduced mass $\mu = m_{\text{AM}} m_{\text{He}}/(m_{\text{AM}} + m_{\text{He}})$ computed from atomic masses in the relative kinetic energy operator.

In the simulation no external magnetic field is applied. Hence, we can assume that the eight hyperfine states of the electronic ground state of $^7$Li and $^{87}$Rb are equally populated. For our purposes, we can also ignore the $R$ dependence of the hyperfine energies of the alkali-metal atoms. Hence, the differential cross sections are the same for all hyperfine states of the alkali-metal atom.

Figure 2 shows $d\sigma_{\text{AM-He}}/d\Omega$ as a function of collision angle $\theta_c$ up to $10°$ for selected collision energies between $E/k = 5$ mK and 500 K. Figure 2(a) shows data for the $^7$Li-$^4$He collision, while Fig. 2(b) shows data for $^{87}$Rb-$^4$He. For an isotropic potential, the differential cross section is independent of $\varphi_c$. The relative uncertainty of differential cross sections is below 5% for $E/k > 40$ K. For $E/k < 0.1$ K it is larger than 20%.
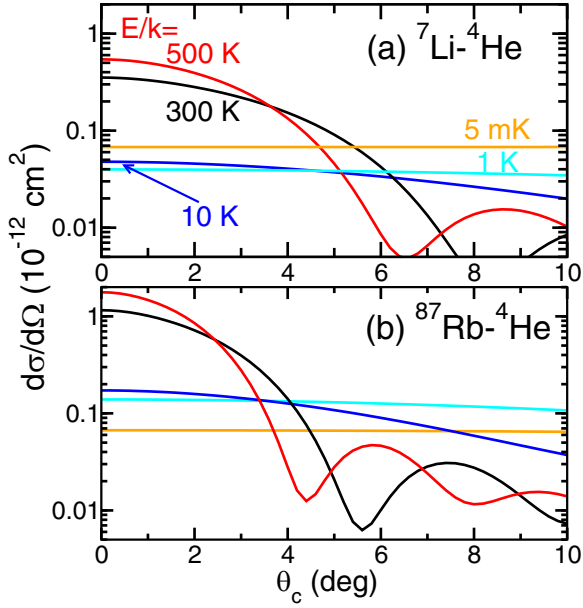
FIG. 2. Differential cross sections $d\sigma_{\text{AM-He}}/d\Omega$ for (a) $^7\text{Li} + {}^4\text{He}$ and (b) $^{87}\text{Rb} + {}^4\text{He}$ as functions of collision angle $\theta_c$ for five relative kinetic energies $E$. The collision energies for the colored curves are the same in the two panels.

We observed that for the largest collision energies shown in Fig. 2 the differential cross section drops off rapidly with angle $\theta_c$. For example, for $E/k \geqslant 10$ K the half width at half maximum is less than a few degrees. For much smaller collision energies, the differential cross section is independent of $\theta_c$. In other words, during the initial cooling process the alkali-metal atoms undergo only small deflections when colliding with helium atoms.

The angular dependence of $d\sigma_{\text{AM-He}}/d\Omega$ can mostly be understood from the long-range dispersion or van der Waals $-C_6/R^6$ behavior of the $X\,^2\Sigma^+$ potential, where the positive $C_6$ is the van der Waals dispersion coefficient. The dispersion interaction introduces natural length and energy scales. These are the van der Waals length $x_6 = \sqrt[4]{2\mu C_6/\hbar^2}$ and van der Waals energy $E_6 = \hbar^2/2\mu x_6^2$. With the dispersion coefficients from Ref. [55], we find $x_6 = 21.4a_0$ and $28.0a_0$ for $^7\text{Li} + {}^4\text{He}$ and $^{87}\text{Rb} + {}^4\text{He}$, respectively, where $a_0 = 0.052\,917\,7$ nm is the Bohr radius. Similarly, $E_6/k = 74$ and 29 mK, respectively.

For collision energies $E \ll E_6$, only a single partial wave, the so-called s wave, contributes to $d\sigma_{\text{AM-He}}/d\Omega$ and we enter the Wigner threshold regime. Then $d\sigma_{\text{AM-He}}/d\Omega \to a^2$ is independent of $\theta_c$, where $a$ is the scattering length. For collision energies $E \gg E_6$, a semiclassical approximation [51] gives a qualitative expression for the differential cross section at small scattering angles $\theta_c \ll \pi$. In fact, we have

$$\frac{d\sigma_{\text{AM-He}}}{d\Omega} = f_0(E/E_6)^{3/5}[1 - f_1(E/E_6)^{4/5}(\theta_c/2)^2]x_6^2, \quad (11)$$

with constants $f_0 = 0.363\,046\ldots$ and $f_1 = 2.018\,179\ldots$ leading to a sharply peaked differential cross section. Still, a comparison with the quantum results in Fig. 2 (not shown) finds that the semiclassical model overestimates $d\sigma_{\text{AM-He}}/d\Omega$

at $\theta_c = 0$ by a factor of 2, while it underestimates the half width at half maximum by a similar factor.

### C. Monte Carlo simulation of the cooling of alkali-metal atoms

The Monte Carlo simulations begin by generating a $^7\text{Li}$ or $^{87}\text{Rb}$ particle at the center of the aperture in front of the alkali-metal source. The particle's velocity $\vec{v}_{\text{AM}}$ is sampled from a Maxwell-Boltzmann distribution for an effusive source at temperature $T_{\text{AM}}$ [47,56] with probability distribution for its speed $v_{\text{AM}} = |\vec{v}_{\text{AM}}|$ given by

$$f_{\text{AM}}(v_{\text{AM}}) = \frac{1}{2}\left(\frac{m_{\text{AM}}}{kT_{\text{AM}}}\right)^2 v_{\text{AM}}^3 \exp\left(-\frac{1}{2}\frac{m_{\text{AM}}v_{\text{AM}}^2}{kT_{\text{AM}}}\right), \quad (12)$$

with $\int_0^\infty dv\, f_{\text{AM}}(v) = 1$ and angular velocity probability distribution given by $\xi(\theta, \varphi) = \cos(\theta)/\mathcal{N}(t_{\text{AMS}})$ for $0 \leqslant \theta \leqslant \pi/(2t_{\text{AMS}})$ and zero otherwise with respect to the $(0, \sin\theta_S, \cos\theta_S)$ direction. Here $m_{\text{AM}}$ is the mass of the alkali-metal atom and $\mathcal{N}(t_{\text{AMS}})$ is defined such that $\int_0^\pi \sin\theta\, d\theta \int_0^{2\pi} d\varphi\, \xi(\theta, \varphi) = 1$. For the aperture in front of our alkali-metal source $t_{\text{AMS}} = \pi/0.18$ or $2t_{\text{AMS}}/\pi = 0.09$. As the diameter of the aperture of the atomic source is small compared to the distance an alkali-metal atom travels before it enters the $^4\text{He}$ jet, we can omit sampling over the initial location of the alkali-metal atom.

Once the initial position and velocity of the $^7\text{Li}$ or $^{87}\text{Rb}$ atom are generated, the particle is propagated through the helium jet with variable time steps $\Delta t$, which are small fractions of the local mean free time for collisions with $^4\text{He}$ atoms. For much of the slowing process, the alkali-metal atom's kinetic energy is large compared to $m_{\text{He}}v_{\text{He,tv}}^2/2$ and $kT_{\text{He}}(r)$ of the helium atoms. This allows us to estimate the local mean free time for an alkali-metal atom at position $\vec{r}_{\text{AM}}$ and velocity $\vec{v}_{\text{AM}}$ in this regime without the need for sampling the thermal distribution of the helium atoms and computing the local rate coefficient $K(\vec{r}_{\text{AM}}, \vec{v}_{\text{AM}}) = \langle v_{\text{rel}}\sigma_{\text{AM-He}}(E)\rangle$, where the angular brackets indicate an average over the velocity distribution of the $^4\text{He}$ atoms only, the relative velocity $\vec{v}_{\text{rel}} = \vec{v}_{\text{AM}} - \vec{v}_{\text{He}}$, and $E = \mu v_{\text{rel}}^2/2$. The mean free time is then well approximated by

$$\tau(\vec{r}_{\text{AM}}, \vec{v}_{\text{AM}}) \approx \frac{1}{n_{\text{He}}(\vec{r}_{\text{AM}})v_{\text{approx}}\,\sigma_{\text{AM-He}}(E_{\text{approx}})}, \quad (13)$$

where

$$v_{\text{approx}} = |\vec{v}_{\text{AM}} - v_{\text{He,tv}}\hat{r}_{\text{AM}}| \quad (14)$$

and $E_{\text{approx}} = \mu v_{\text{approx}}^2/2$. Once the velocity of an alkali-metal atom approaches the approximately 210 m/s terminal velocity of the helium atoms, Eq. (13) loses accuracy. Hence, for $|\vec{v}_{\text{AM}} - v_{\text{He,tv}}\hat{r}_{\text{AM}}| < v_{\text{cutoff}}$, where $v_{\text{cutoff}} = 50$ m/s, the mean free time at $\vec{r}_{\text{AM}}$ and $\vec{v}_{\text{AM}}$ is evaluated exactly with

$$\tau(\vec{r}_{\text{AM}}, \vec{v}_{\text{AM}}) = \frac{1}{n_{\text{He}}(\vec{r}_{\text{AM}})K(\vec{r}_{\text{AM}}, \vec{v}_{\text{AM}})} \quad (15)$$

and

$$K(\vec{r}_{\text{AM}}, \vec{v}_{\text{AM}}) = \int d^3v_{\text{He}}\, v_{\text{rel}}\sigma_{\text{AM-He}}(E)\frac{P_{\text{He}}(\vec{r}_{\text{AM}}, \vec{v}_{\text{He}})}{p_{\text{He}}(\vec{r}_{\text{AM}})}$$

$$= \mathcal{K}(|\vec{v}_{\text{AM}} - v_{\text{He,tv}}\hat{r}_{\text{AM}}|, T_{\text{He}}(r_{\text{AM}})), \quad (16)$$

where

$$\mathcal{K}(v, T) = 4\pi \left( \frac{m_{\text{He}}}{2\pi kT} \right)^{3/2} e^{-m_{\text{He}}v^2/(2kT)}$$
$$\times \int_0^\infty v_{\text{rel}}^2 dv_{\text{rel}} [v_{\text{rel}} \sigma_{\text{AM-He}}(E)]$$
$$\times e^{-m_{\text{He}}v_{\text{rel}}^2/(2kT)} \frac{\sinh(m_{\text{He}}v_{\text{rel}}v/kT)}{m_{\text{He}}v_{\text{rel}}v/kT}. \quad (17)$$

Here $K(\vec{r}_{\text{AM}}, \vec{v}_{\text{AM}})$ is only a function of the local speed of the alkali-metal atom in the frame moving along with velocity $v_{\text{He,tv}} \hat{r}_{\text{AM}}$ and the local helium temperature $T_{\text{He}}(r_{\text{AM}})$. For fast evaluation, the rate coefficient $\mathcal{K}(v, T)$ is precomputed on a grid of $T$ from 0.1 to 100 mK and $v$ from 0 m/s to $v_{\text{cutoff}}$. A two-dimensional interpolator is then used to determine $\mathcal{K}(v, T)$ at any $v$ and $T$ within the boundary of the grid. The grid size is chosen such that the difference between the interpolated value and that from numerical integration of Eq. (16) is less than 1%. Moreover, the difference between Eqs. (13) and (15) is less than 2% for $v > v_{\text{cutoff}}$ and $T_{\text{He}} < 100$ mK.

We use an acceptance-rejection procedure to determine whether an alkali-metal atom, located at phase-space point $(\vec{r}_{\text{AM}}, \vec{v}_{\text{AM}})$, collides with a $^4$He atom. The procedure starts by computing the local mean free time $\tau_l$ and equate time step $\Delta t$ to the preliminary value $s\tau_l$ with $0 < s \ll 1$. Our value for $s$ is discussed below. The time step $\Delta t$ is adjusted if one of two conditions is met. First, if $v_{\text{AM}}\Delta t > \Delta S$ for distance $\Delta S$ discussed below, we set $\Delta t = \Delta S/v_{\text{AM}}$. We then compute $\tau_n$, the local mean free time at the "next" phase-space position $(\vec{r}_{\text{AM}} + \vec{v}_{\text{AM}}\Delta t, \vec{v}_{\text{AM}})$, and if $\tau_l \geqslant 2\tau_n$ we half $\Delta t$ and the process of adjusting $\Delta t$ repeats. The process halts when neither inequality is met and we accept $\Delta t$. We observe that $s\tau_l$ is the upper bound to the accepted time step.

The constraint $v_{\text{AM}}\Delta t < \Delta S$ is required as alkali-metal atoms entering the jet far from the jet nozzle are in regions of relatively low $^4$He number density. Using only the local mean free time to determine $\Delta t$ can incorrectly result in a particle traveling through the jet without undergoing collisions.

Finally, the probability of a collision between an alkali-metal atom and a $^4$He atom is $p_{\text{AM}} = (1/\tau_l + 1/\tau_n)\Delta t/2$. In our simulations, we use $s = 0.1$ and $\Delta S = 1$ mm. These values for $s$ and $\Delta S$ ensure that the likelihood of a collision is always less that 15% and that we can compute sufficiently accurate statistical averages within a reasonable amount of time on the computational resources available to us.

A random number $\mathcal{P}$ between 0 and 1 is now generated from the uniform probability distribution. If $\mathcal{P} \geqslant p_{\text{AM}}$ then the alkali-metal atom moves from $(\vec{r}_{\text{AM}}, \vec{v}_{\text{AM}})$ to $(\vec{r}_{\text{AM}} + \vec{v}_{\text{AM}}\Delta t, \vec{v}_{\text{AM}})$. If $\mathcal{P} < p_{\text{AM}}$ an AM-$^4$He collision occurs at $(\vec{r}_{\text{AM}}, \vec{v}_{\text{AM}})$.

When a collision with a $^4$He atom occurs, we generate a helium velocity $\vec{v}$ sampled from distribution $P_{\text{He}}(\vec{r}_{\text{AM}}, \vec{v})$ in Eq. (1) for velocities $|\vec{v}_{\text{AM}} - v_{\text{He,tv}} \hat{r}_{\text{AM}}| > v_{\text{cutoff}}$, while for other velocities we sample from $v_{\text{rel}}\sigma_{\text{AM-He}}(E)P_{\text{He}}(\vec{r}_{\text{AM}}, \vec{v})$. This latter sampling technique is the DBRC algorithm described in Ref. [57] and favors $^4$He velocities where $v_{\text{rel}}\sigma_{\text{AM-He}}(E)$ is large.

Collisions change the velocities of the atoms conserving the center-of-mass velocity $\vec{v}_{\text{c.m.}}$ and the magnitude of the relative velocity $v_{\text{rel}} = |\vec{v}_{\text{rel}}|$ while keeping the atoms at the same location $\vec{r}_{\text{AM}}$. The final velocities $\vec{w}_{\text{AM}}$ and $\vec{w}$ postcollision for the alkali-metal atom and $^4$He, respectively, are most conveniently evaluated in center-of-mass and relative coordinates with scattering angle $\theta_c \in [0, \pi]$ sampled from $\sin\theta_c d\sigma_{\text{AM-He}}/d\Omega$ at the relative collision energy $E = \mu v_{\text{rel}}^2/2$ and azimuthal angle $\varphi_c$ uniformly sampled from $[0, 2\pi]$. Some thought then shows that the final velocity of the alkali-metal atom is $\vec{w}_{\text{AM}} = \mu\vec{w}_{\text{rel}}/m_{\text{AM}} + \vec{v}_{\text{c.m.}}$, where the final relative velocity

$$\vec{w}_{\text{rel}} = (\sin\theta_c \cos\varphi_c \hat{x}' + \sin\theta_c \sin\varphi_c \hat{y}' + \cos\theta_c \hat{z}')v_{\text{rel}}, \quad (18)$$

with unit vector $\hat{z}' = \hat{v}_{\text{rel}} = (n_{\text{rel},x}, n_{\text{rel},y}, n_{\text{rel},z})$ parallel to the initial relative velocity and unit vector $\hat{x}' = (-n_{\text{rel},y}, n_{\text{rel},x}, 0)/\sqrt{n_{\text{rel},x}^2 + n_{\text{rel},y}^2}$ perpendicular to $\hat{z}'$. Finally, unit vector $\hat{y}' = \hat{z}' \times \hat{x}'$ so that the three unit vectors form a positively oriented orthonormal basis.

The steps of the simulation are then repeated until the particle leaves our spatial bounds, which are typically $x \in [-6 \text{ cm}, 6 \text{ cm}]$, $y \in [-6 \text{ cm}, 6 \text{ cm}]$, and $z \in [-4 \text{ cm}, 10 \text{ cm}]$. The net result is an ensemble of computed trajectories from which observable quantities can be calculated. The number of computed trajectories $N$ varies from a few $10^6$ to $100 \times 10^6$ for converged results. A larger $N$ is required for smaller spatial regions or velocity intervals. The simulation is written in PYTHON and utilizes the NUMBA library for optimized performance [58].

## III. RESULTS

### A. Seeding with $^7$Li

The trajectory of a seeded $^7$Li atom which exits the skimmer along $(x, y) \approx (0, 0)$ projected onto the $(y, z)$ plane is shown in the top panel of Fig. 3 for a $^4$He flow rate of 200 SCCM (where SCCM denotes cubic centimeter per minute at STP). Here a $^4$He flow rate of 1 SCCM corresponds to $\dot{N}_0 = 4.48 \times 10^{17}$ s$^{-1}$. (The term standard in the unit SCCM reflects standard conditions for temperature and pressure of 273.15 K and 101.325 kPa, respectively.) The use of the unit SCCM for specifying helium flow rate is due to standard terminology in the field. The six panels at the bottom of Fig. 3 show distributions of the kinetic energy $E = m_{\text{Li}}(\vec{v}_{\text{Li}} - v_{\text{He,tv}}\hat{r})^2/2$ of $^7$Li atoms in the frame moving along with the local terminal velocity of helium atoms in the jet. Each panel shows a distribution of kinetic energies of atoms as they pass through a rectangular region perpendicular to and centered on points along the trajectory in the top panel of Fig. 3. The region extends by $\pm 0.1$ cm into the $x$ direction. Its length in the $(y, z)$ plane is 0.4 cm.

The distribution of kinetic energies as the $^7$Li atoms pass through area L1 and begin to enter the jet is close to a Maxwell-Boltzmann distribution with a temperature of 800 K, equal to the effusive source temperature. At the third region, a small second peak at $E/k \approx 10$ mK appears, indicating that $^7$Li atoms are becoming trapped in the jet. This second peak becomes more pronounced for the last three positions along the trajectory with its peak position shifting to a smaller $E$. The seeded $^7$Li atoms are getting colder. It should be recognized that as the L$j$ have a finite area, the increasing prominence of the peak near $E/k \approx 1$ mK relative to those at
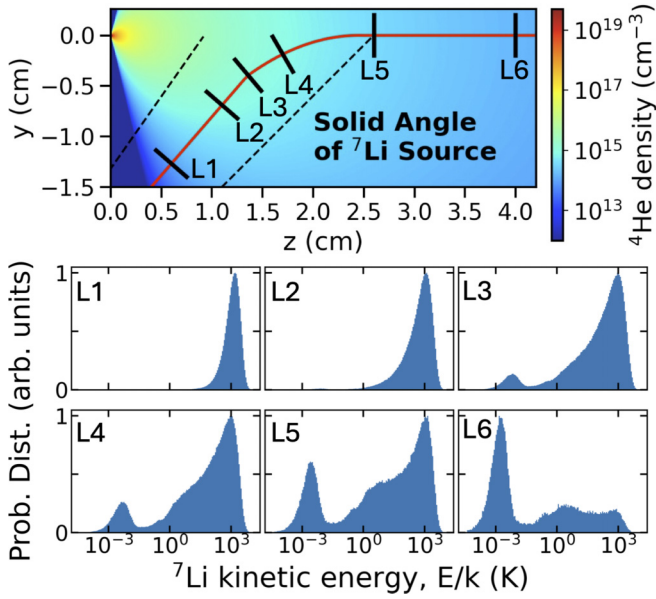
FIG. 3. Shown on top is the trajectory of a seeded $^7$Li atom (red curve) from our 3D Monte Carlo simulations overlaid on a 2D cut through the number density profile of the $^4$He jet for the $(0, y, z)$ plane. The dashed lines indicate the solid angle within which most $^7$Li atoms from the atomic oven enter our simulation region. The bottom panels labeled L$j$, with $j = 1, 2, 3, 4, 5$, and 6, show the $^7$Li number probability distributions as functions of the $^7$Li kinetic energy in a moving frame of the $^4$He jet for various small areas L$j$ along but perpendicular to the trajectory shown in the top panel. The vertical axes of the six panels are all scaled to a height of one.

higher kinetic energies cannot used to estimate the jet seeding efficiency.

Figure 4 shows several cuts through simulated three-dimensional $^7$Li velocity distribution at a distance of 10 cm from the sonic nozzle along the centerline of the jet and with a
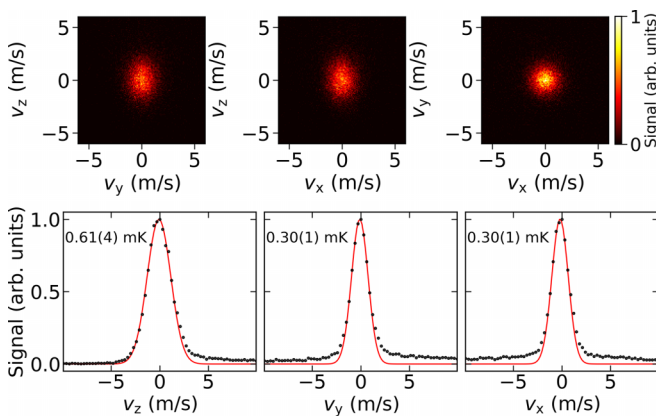


FIG. 4. Contour and line graphs of 2D and 1D cuts through the 3D $^7$Li velocity distributions relative to the terminal velocity of the helium jet. Results are shown for particles passing within a 1-mm-radius circle perpendicular to the centerline of the helium jet at a distance of 10 cm from the helium nozzle. Gaussian profiles (red curves) are fit to the FWHM of the central peak. For each line graph, the fitted standard deviation of the velocity distribution $v_{\mathrm{fit}}$ is specified as $T_{\mathrm{fit}} = m_{\mathrm{Li}} v_{\mathrm{fit}}^2 / (2k)$.


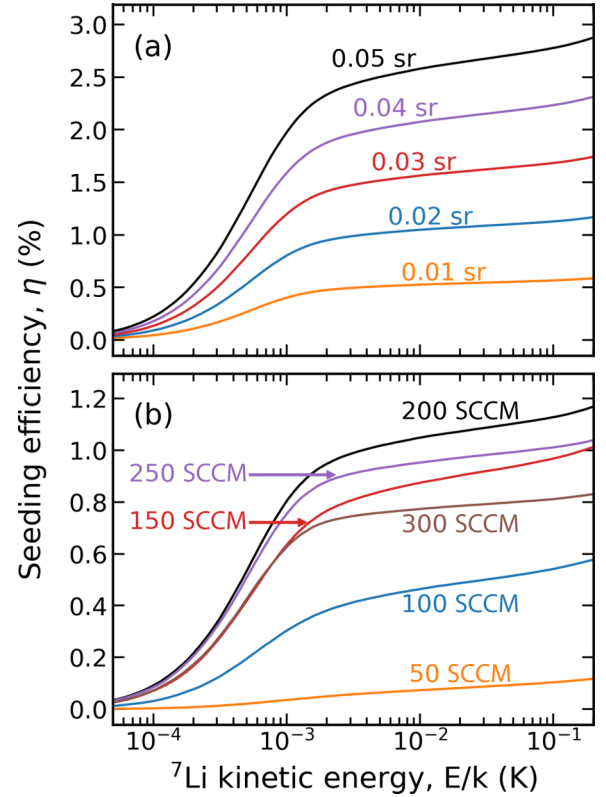
FIG. 5. Percentage of simulated $^7$Li atoms with energy in the moving frame up to the value specified on the $x$ axis. Results are at a distance of 10 cm from the sonic nozzle with the solid angle defined relative to the location of the sonic nozzle. (a) Results for various solid angles with a helium flow rate of 200 SCCM. (b) Results for various helium flow rates and a solid angle of 0.02 sr.

$^4$He flow rate of 200 SCCM. The atoms are nearly thermalized with the helium jet but still exhibit some asymmetry in the $v_z$ and $v_y$ distributions and have wings which extend to larger distances than what a Maxwell-Boltzmann distribution would yield. Nevertheless, we can define an effective temperature for the seeded atoms by fitting the central peaks to Gaussian distributions as shown in Fig. 4. It is desirable to know what percentage of the injected $^7$Li atoms cool to these effective temperatures. For this we quantify the cumulative fraction of total simulated particles with a kinetic energy in the moving frame less than a specified value $E$. We define the seeding efficiency $\eta(E, \Omega)$ as this fraction of particles which are also directed within a solid angle $\Omega = \pi r^2 / L^2$, i.e., through a circle of radius $r$ centered on the beam axis at a distance $L$ from the nozzle.

In Fig. 5 the seeding efficiency is given for a variety of flow rates and solid angles at a distance of $L = 10$ cm from the nozzle as most of the cooling has occurred by this point. Additional discussion of cooling versus distance from the nozzle can be found in the Appendix. For our source geometry, the skimmer can extract atoms within a solid angle of approximately 0.02 sr. As simulations show that the seeding efficiency increases with a solid angle, a larger extractable flux could be obtained with a different skimmer geometry. However, this also results in a larger flux of helium atoms leaving the skimmer. In practice, careful consideration should
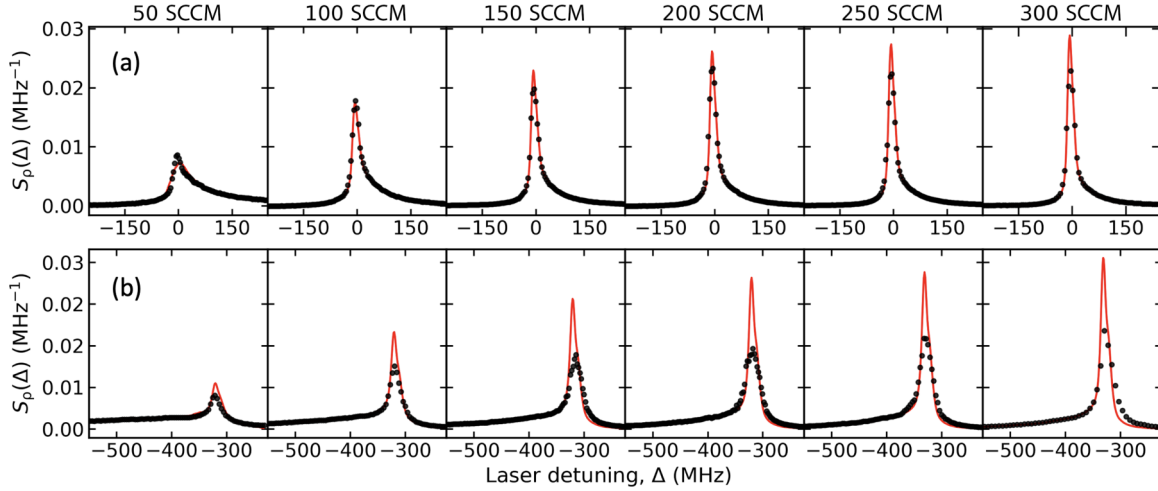
FIG. 6. Experimental $^7$Li fluorescence spectra (black markers) and simulated spectra (red curves) as functions of the laser detuning $\Delta$ from the average transition frequency of the $F = 2$ to $F' = 1, 2, 3$ transitions of the $D_2$ line of $^7$Li weighted by the respective transition strengths: (a) transverse spectra taken 4.1 cm downstream from the nozzle and (b) longitudinal spectra. From left to right, spectra are taken for six increasing $^4$He flow rates, indicated above the top row in units of SCCM.

be taken to ensure acceptable vacuum pressures outside the cryogenic region.

### B. Comparison with $^7$Li experiments

In the experimental realization, studied in Ref. [12], local $^7$Li density and velocity distributions were determined with fluorescence spectroscopy on transitions between magnetic sublevels of the $F = 2$ hyperfine state of the electronic $1s^2 2s(^2S)$ ground state to three of the four hyperfine components $F'$ of the excited $1s^2 2p(^2P_{3/2})$ state. We measure laser-induced fluorescence as a function of laser frequency $\nu$ with either a linearly polarized probe laser parallel to the centerline of the jet and propagation direction $-\hat{z}$ (laser beam $\rho = \parallel$) or a linearly polarized probe laser perpendicular to the centerline and propagation direction $+\hat{y}$ (laser beam $\rho = \perp$). The laser perpendicular to the jet is located 4.1 cm from the sonic nozzle.

In our simulations, the laser spatial intensity profile $I_\rho(\vec{r})$ of lasers $\rho = \parallel$ and $\perp$, propagating parallel and perpendicular to the centerline of the jet, respectively, are modeled as rectangles with a width along $x$ equal to twice the beam waist $w_0 = 0.41$ cm in their propagation direction. The height of the rectangle along $y$ is generally chosen to be small such that variations in the laser intensity can be neglected. Inside the rectangle, the intensity is constant, while outside it is zero. Moreover, the lasers operate at sufficiently low intensities $I/I_{\mathrm{sat}} < 0.04$ that optical pumping effects are negligible.

From the ensemble of trajectories, we compute the distribution $P_{\mathrm{AM}}(x, y, \vec{v}_{\mathrm{AM}})$ of positions $x$ and $y$ at which particles pass through a surface perpendicular to the jet axis at a distance $L$ from the nozzle, with $\vec{v}_{\mathrm{AM}}$ their velocity at that position. The simulated spectral profile for laser beam $\rho$ is

$$S_\rho(\Delta) = \kappa \int_A dx\, dy \int d^3 \vec{v}_{\mathrm{AM}} P_{\mathrm{AM}}(x, y, \vec{v}_{\mathrm{AM}}) W_\rho(\vec{v}_{\mathrm{AM}}) \sum_{F'=1}^{3}$$

$$\times \frac{D_{F'} I_\rho(\vec{r}_{\mathrm{AM}})}{1 + 4[\Delta - \vec{k}_\rho \cdot \vec{v}_{\mathrm{AM}}/(2\pi) - \Delta_{\mathrm{hf}}(F')]^2/\gamma^2}, \quad (19)$$

where $\kappa$ is a constant of proportionality. Since we do not simulate absolute signal levels obtained on our camera, we adjust $\kappa$ such that $\int S_\rho(\Delta) d\Delta = 1$ for both experiment and simulation. Here $\Delta = \nu - E_{D2}/h$ is the laser detuning from the average transition frequency from $F = 2$ to $F' = 1, 2, 3$ weighted by the respective transition strength. The interrogation area $A$ is a rectangle with a height equal to 0.60(2) mm. The width is equal to the laser beam waist. We find that results are insensitive to variations in the width of the rectangle indicating negligible variations in the velocity profiles $v_y$ and $v_z$ along $x$. Here $h$ is the Planck constant. Moreover, the sum is over the optically allowed hyperfine levels $F'$ of the $1s^2 2p(^2P_{3/2})$ state and $\Delta_{\mathrm{hf}}(F') = +9.619, +3.730$, and $-5.656$ MHz are hyperfine frequency shifts for the $F' = 1, 2$, and 3 levels of the $^7$Li $1s^2 2p(^2P_{3/2})$ state, respectively [59]. The relative strengths $D_{F'}$ are $1/20, 1/4$, and $7/10$ for $F' = 1, 2$, and 3, respectively, to account for the different line strengths of the $F = 2$ to $F'$ transitions. The natural linewidth of the $^7$Li $1s^2 2p(^2P_{3/2})$ state is $\gamma = 5.87$ MHz [60]. We do not include contributions from our laser linewidth over the interrogation time of the atoms (less than 2 MHz FWHM) in our model as it is much smaller than the Doppler widths and natural linewidth.

The inner product $\vec{k}_\rho \cdot \vec{v}_{\mathrm{AM}}$ in Eq. (19) accounts for Doppler shifts. Here the unit vector $\hat{k}_\rho = \vec{k}_\rho/k_\rho$ gives the direction of the laser $\rho$ and the wave number $k_\rho$ is given by the dispersion relation $h\nu = \hbar c k_\rho$ with speed of light in vacuum $c$ and reduced Planck constant $\hbar$. As shown in Fig. 6 for laser beam $\rho = \parallel$, $k_{\parallel} v_{\mathrm{He,tv}}/(2\pi) = 310$ MHz, which yields a forward velocity of approximately 210 m/s. The weight function $W_\rho(\vec{v}_{\mathrm{AM}})$ in Eq. (19) accounts for the reduced number of fluorescence photons emitted from faster-moving atoms that spend less time in the laser beam. For both parallel and perpendicular lasers, we use $W_\rho(\vec{v}_{\mathrm{AM}}) = 1/v_{\mathrm{AM}}$ as the detected volume 4.1 cm from the sonic nozzle is small.

Line shapes for both experiment and simulation are given in Fig. 6. Line shapes at this distance show a clear asymmetry. Simulated profiles reproduce the measured asymmetry while also predicting a narrower central peak. For the

longitudinal profiles, we estimate an optical density of approximately 0.3 over the distance of our chamber (approximately 2 m). The non-negligible absorption effects may in part explain the larger discrepancy for the longitudinal profiles.

A point of interest in our apparatus is maximizing seeded lithium that is extracted by our skimmer as shown in Fig. 1. The experimentally measured $^7$Li density, described in Ref. [12], is compared to that obtained through simulation by measuring the injected lithium flux with zero helium flow. This allows us to compute the average simulated alkali-metal-atom number density that is within the projected area $A$ of the skimmer using

$$n_{\mathrm{sim}} = \frac{\Phi}{NA} \sum_i^{N_c} \frac{1}{v_i}, \tag{20}$$

where $\Phi$ is the measured experimental alkali-metal-atom flux entering the cryogenic region, $N$ is the total number of simulated alkali-metal particles, $v_i$ is the speed of simulated particles within the capture region, and $N_c$ is the number of simulated particles within $A$. We compare the simulated and measured total densities at all velocities as experimental measurements cannot distinguish if an atom is within a narrow velocity range in both the transverse and longitudinal directions.

Results using our transverse probe for a variety of helium flow rates at a distance of 4.1 cm from the nozzle are given in Fig. 7. At this distance, the projection of the skimmer corresponds to a circle of radius approximately equal to 0.33 cm. In Fig. 7(a) the number density for a circle centered at $(x, y) = (0, 0)$ is given with the simulation correctly predicting a maximum average density at a helium flow rate of 150 SCCM. This result may appear to contradict the seeding efficiencies given in Fig. 5; however, it is important to note that the simulated and experimentally measured densities include all velocity classes extending well past the values shown in Fig. 5. While a flow rate of 150 SCCM results in a larger density within $A$, the simulation predicts that a flow rate of 200 SCCM results in more seeded atoms with lower energies in the moving frame.

Shown in Fig. 7(b) is the number density but with the circle centered at the location of the peak density along $y$ with $x = 0$. For flow rates below approximately 150 SCCM the location of the peak number density occurs above the centerline of the jet, while for flow rates above approximately 150 SCCM it occurs below the centerline. Since the helium density along $y$ is largest at $y = 0$, it may initially seem surprising that the location of the peak $^7$Li density is not necessarily located at $y = 0$. This effect of helium flow rate on the position of the extractable lithium atoms is best visualized by examining the position of simulated particles. The positions of all particles which pass the $(x, y)$ plane 4.1 cm in front of the nozzle are given by Fig. 8(a). At the highest flow rates particles are being deflected by the jet, while at the lowest flow rate the shadow of particles exiting the aperture in front of the oven is visible. In Fig. 8(b) we show the position of only particles with energies less than or equal to $k \times 50$ mK in the moving frame. Notably, if one wishes to maximize the extraction of thermalized lithium, it would be advantageous to extract not at the centerline of the jet but beneath it.
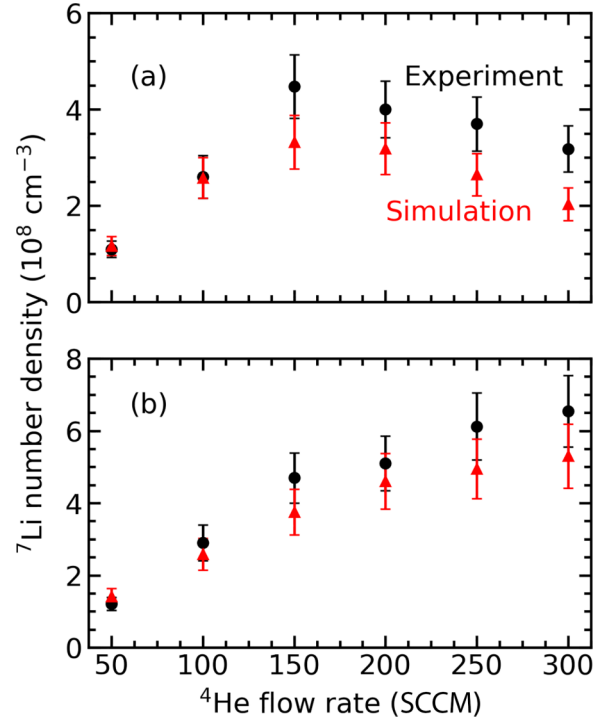


FIG. 7. Measured (black circles) and modeled (red triangles) average $^7$Li number densities $n_{\mathrm{Li}}$ at 4.1 cm from the nozzle within a circle of radius approximately equal to 0.33 cm as functions of helium flow rate. Results corresponds to (a) a circle centered at $(x, y) = (0, 0)$ and (b) a circle centered at the location of the peak number density along $y$ with $x = 0$. The terminal velocity of the lithium beam is 210(2) m/s for a helium flow rate below 220 SCCM and 217(2) above 220 SCCM. The simulated $^7$Li number densities follow from the measured flux leaving the lithium source of $1.4(2) \times 10^{14}$ s$^{-1}$ at a lithium oven temperature of 800 K. Error bars represent one standard deviation of uncertainty.

For all simulated density results, we find that the uncertainties of the capture rates obtained with our MC results are larger than those of the differential cross sections. This simply reflects the small theoretical uncertainties in the differential cross section for $E/k > 10$ K.

Due to the large reservoir of helium, we assume no appreciable heating of the jet and expect this to hold true for sufficiently low lithium flux. For reference, with a seeded flux on the order of $10^{14}$ s$^{-1}$, there are approximately 500 000 helium atoms per lithium atom for 150 SCCM of helium flow. For an oven temperature of 800 K, the average energy of a lithium atom entering the jet is approximately $k \times 1070$ K. If this energy were uniformly distributed among the helium atoms it would deposit only $k \times 2$ mK per helium atom. To further examine how energy is deposited in the jet we record the location as well as the pre- and postcollision velocities of the lithium and helium. A map of the energy deposition can then be constructed and is given by Fig. 9(a), which shows that most of the energy deposited by the lithium is deposited before the lithium reaches the center of the jet.

Naively, it might seem like a large fraction of energy that is deposited in the periphery of the jet would remain there as the
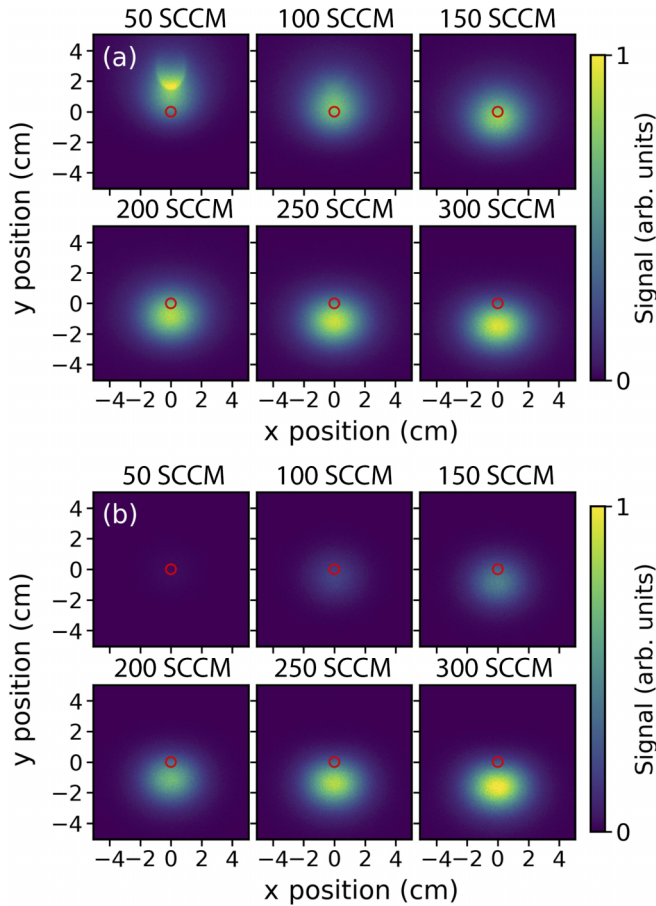
FIG. 8. 2D histogram of the positions of simulated $^7$Li atoms that pass the $(x, y)$ plane 4.1 cm from the nozzle. The red circle indicates particles that are within the projection of the skimmer. The numbers above each plot indicates the $^4$He flow rate. (a) Results for all $^7$Li energies in the moving frame. (b) Results for $^7$Li energies less than or equal to $k \times 50$ mK in the moving frame.

jet expands. This would limit heating effects along the center of the expansion. However, we have examined this further and found that it is only partially true. Depending on the energy transferred from the lithium atom and scattering angles, an energetic helium atom can have a significantly larger mean free path relative to the local mean free path of less energetic helium atoms.

To quantify this effect, the simulation is repeated using the location and postcollision velocity of the helium within the blue square in Fig. 9 using the $^4$He-$^4$He cross section from Ref. [46]. The helium atoms then travel until they leave the simulation bounds or undergo a single collision. Figure 9(b) shows the energy deposition for this group of helium atoms. Helium atoms containing approximately 30% of the energy deposited in the blue square leave the simulation bounds without undergoing further collisions. While this method does not allow us to determine how the remainder of the energy is ultimately distributed in the jet, it illustrates that a non-negligible amount of energy is effectively removed. It also suggests that heating of the center of the jet can come from energy that is initially deposited in the periphery. For sufficiently high lithium flux there will be heating of the jet
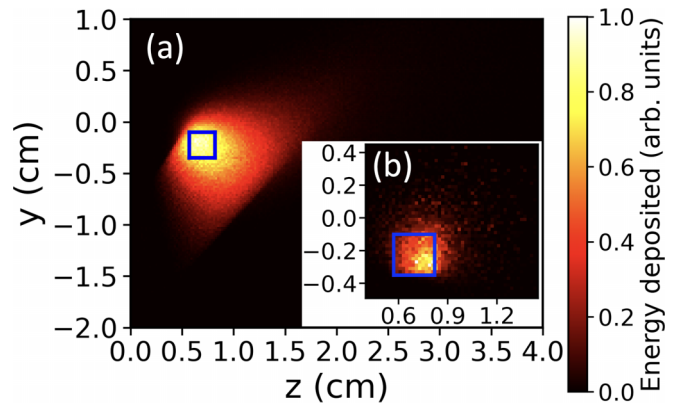


FIG. 9. (a) Location and relative magnitude of energy deposited by $^7$Li atoms from $x = -0.1$ cm to $x = 0.1$ cm. (b) Relative magnitude of energy deposited for the next He-He collision for helium atoms which underwent a collision with a lithium atom in the blue square.

and the assumptions made for the jet density and velocity distributions will no longer be valid. To date, we have been able to seed the jet with a lithium flux on the order of $10^{15}$ s$^{-1}$ and extract a lithium beam with a longitudinal temperature of 7(3) mK and a transverse temperature less than 20 mK [12].

### C. Seeding with $^{87}$Rb

As our method is intended to be applicable for a variety of species, there is interest in examining the efficiency for seeding heavier particles into the jet. Here we present simulations of seeding $^{87}$Rb into the helium jet. We assume the same solid angle as our lithium source but at an oven temperature of 550 K due to rubidium's significantly higher vapor pressure. Due to having a higher initial momentum, seeding becomes more challenging as more collisions are required to thermalize the species into the jet.

Under these conditions, optimal seeding efficiency is found when the collisional thickness is increased by changing the seeding position to 1 cm and increasing the helium flow rate to 300 SCCM.[1] In Fig. 10 the cooling process of rubidium injected into the helium jet is shown. Additionally, the position of all particles that pass the $(x, y)$ plane 4.1 cm in front of the nozzle is shown in Fig. 11. As with lithium, a large distribution of kinetic energies is observed far from the nozzle. However, as the cooling process is slower with respect to distance from the nozzle, a clear central peak around $k \times 1$ mK energy is not observed. This is further reflected in the velocity distributions and velocity phase-space plots given by Fig. 12, where the asymmetry in $v_z$ and $v_y$ prevents reliable fitting to a central peak. The qualitative difference in the shape of the distributions as compared to lithium can be in part understood due to the lower initial speed of the rubidium atoms. The mean speed for a rubidium source at 550 K is 435 m/s, compared to

---

[1]It is possible that a shorter seeding position results in better performance, but we have limited the seeding distance due to practical constraints of the beam source geometry.
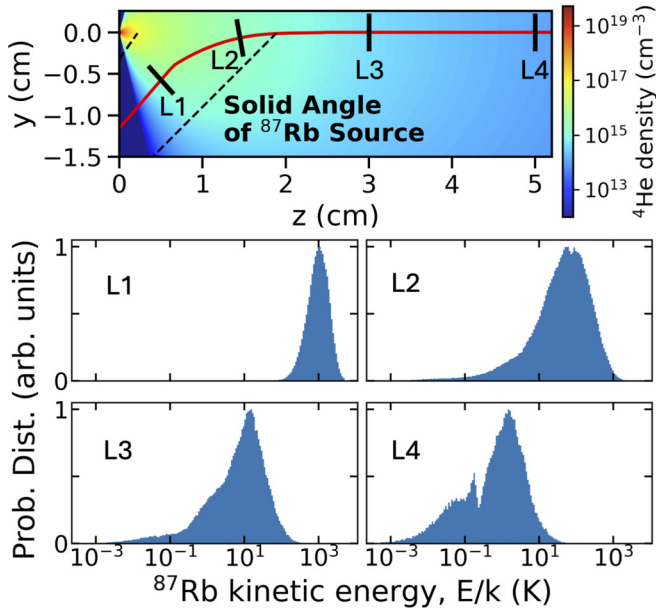
FIG. 10. Shown on top is the trajectory of seeded $^{87}$Rb atoms (red curve) from our 3D Monte Carlo simulations overlaid on a 2D cut through the number density profile of the $^4$He jet at 300 SCCM for the $(0, y, z)$ plane. The sonic nozzle of the $^4$He jet is located at $(y, z) = (0, 0)$. The trajectory has been postselected to lie within planes $x = -0.1$ and $0.1$ cm. The dashed lines indicate the solid angle within which most $^{87}$Rb atoms from the atomic oven enter our simulation region. The bottom panels labeled L$j$, with $j = 1, 2, 3, 4$, show the $^{87}$Rb number probability distributions as functions of the $^{87}$Rb kinetic energy in a moving frame of the $^4$He jet for various small areas L$j$ along but perpendicular to the trajectory shown in the top panel. The vertical axes of the four panels are all scaled to a height of one.

1800 m/s for a lithium source at 800 K. A rubidium atom that is entrained and partially thermalized along the centerline of the jet can remain along the centerline longer than a lithium atom with a higher velocity.

Differences in the velocity distributions of $v_x$, $v_y$, and $v_z$ can be understood by considering geometric constraints. The velocity distributions are analyzed over a 1-mm-radius circle centered at $(x, y) = (0, 0)$. As the atoms are injected from an oven beneath the jet centered at $x = 0$, this sets a limit on the maximum value of $v_x$ for a given initial speed. The
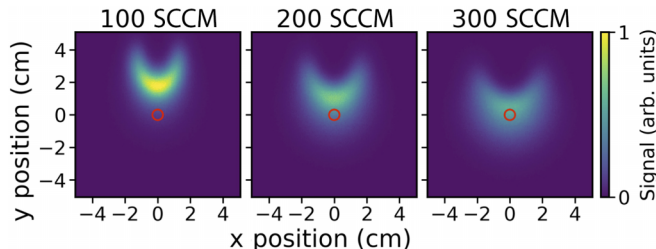


FIG. 11. 2D histogram of the position of simulated $^{87}$Rb atoms that pass the $(x, y)$ plane 4.1 cm from the nozzle. The red circle indicates particles that are within the projection of the skimmer at this distance.
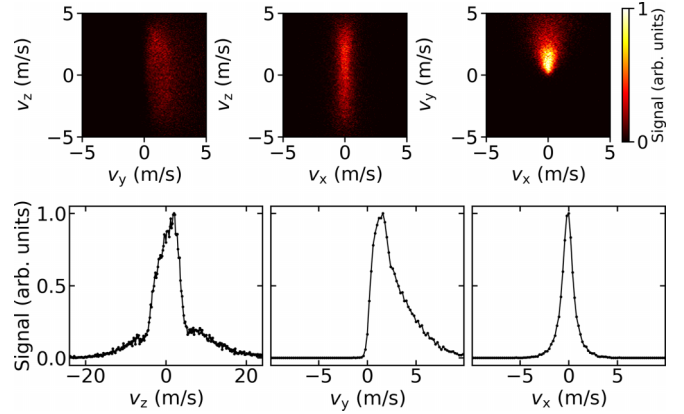


FIG. 12. Contour and line graphs of 2D and 1D cuts through the 3D $^{87}$Rb velocity distributions relative to the terminal velocity of the helium jet. Results are shown for particles passing within a 1-mm-radius circle perpendicular to the centerline of the helium jet at a distance of 10 cm from the helium nozzle.

same constraint does not apply for $v_z$. It is interesting that the distribution for $v_y$ has a sharp cutoff compared to the other two velocity profiles. All rubidium atoms initially have a large $v_y$ in the moving frame. Since the mass of $^{87}$Rb is approximately 20 times larger than that of $^4$He, this ensures that a $^{87}$Rb atom deflected downward has essentially thermalized with the helium. This results in the apparent sharp cutoff and asymmetry as there is a larger distribution of partially thermalized rubidium atoms.

The seeding efficiency for rubidium for a variety of flow rates and solid angles is shown in Fig. 13 for a distance of $L = 10$ cm from the nozzle. If a velocity filter is used to remove faster moving rubidium, then it is predicted that at 300 SCCM of helium flow, approximately 1% of the seeded rubidium would leave the skimmer with energies less than $k \times 75$ mK in the moving frame of the helium.

## IV. CONCLUSION

We have simulated postnozzle seeding into a supersonic helium jet. Conditions that maximize seeded flux agree with experimental measurements as well as provide reasonable agreement to measured spectral profiles. Results show that within a solid angle of 0.02 sr and for energies in the moving frame of the jet of less than $k \times 10$ mK, seeding efficiencies of approximately 1% and approximately 0.2% are possible for lithium and rubidium atoms, respectively. The beams that form have a forward velocity of approximately 210 m/s.

Since seeding of rubidium is indicated, it may be possible to seed other heavier species such as molecules. To achieve efficient seeding, the species would need to have collision cross sections with helium, which increase drastically at low collision energies. All of the alkali-metal atoms have these properties, but it is less clear if this is true for other species. If so, the translational temperatures of such beams could be considerably lower than prior works with seeded jets as well as buffer-gas-based techniques [61], which both generally attain temperatures around 1 K. The monochromaticity of the
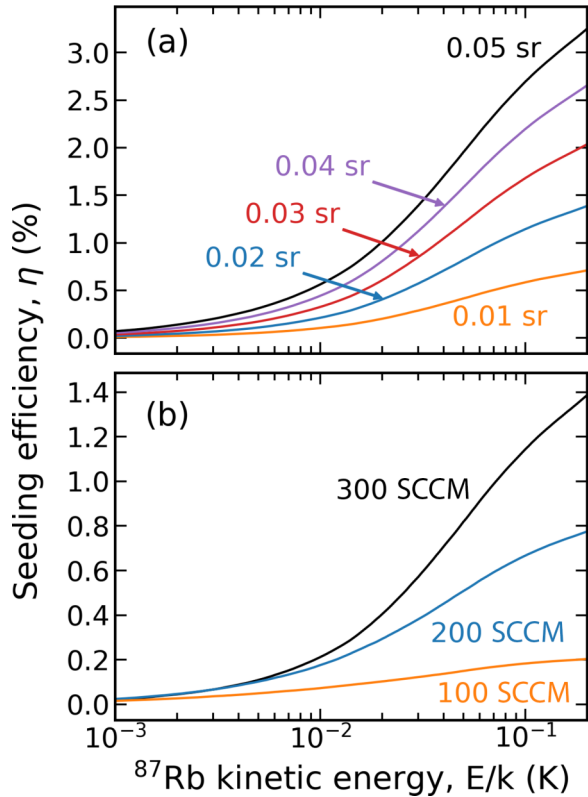
FIG. 13. Percentage of simulated $^{87}$Rb atoms with energy in the moving frame up to the value specified on the $x$ axis. Results are at a distance of 10 cm from the sonic nozzle with the solid angle defined relative to the location of the sonic nozzle. (a) Results for various solid angles with a helium flow rate of 300 SCCM. (b) Results for various helium flow rates and a solid angle of 0.02 sr.

postnozzle seeded beam along with the relatively low forward velocity then makes atom-optical manipulation with a magnetic or electrostatic lens highly efficient [12,62]. The intense beams that form can then be used for studies of cold collisions, atom optics, and precision measurement experiments. Alternatively, cold collision studies can be carried out in the region close to the nozzle. For example, the low collision energies between the seeded alkali-metal atoms and helium would be ideal for studying the formation of weakly bound alkali-metal-atom–helium pairs [27,28].

The simplified model of the jet, while not capturing all relevant features, provides a suitable starting point for understanding seeding dynamics. Extensions of this work could include examining the use of a shaped helium nozzle. Shaped nozzles can increase the intensity of the helium jet [63] and may also increase the seeding efficiency. A 3D direct simulation Monte Carlo approach that simulates the helium jet and lithium beam could be performed to accurately capture the jet dynamics but would be significantly more computationally expensive [43]. It would however allow for a detailed study of heating dynamics. Additionally, adding inelastic collisions to the model would allow for the study of rotational cooling of seeded molecules [16,64].

## APPENDIX: HELIUM JET SIMULATIONS

We have compared our static model for the helium jet to direct-simulation Monte Carlo (DSMC) calculations of helium expansions. These are performed using the DS2V software, a direct-simulation Monte Carlo program written by Bird [65]. For the computational resources available to us, simulations of the helium expansion are limited to source conditions which correspond to substantially lower collision rates than what is expected in our system. Furthermore, the simulations begin at the opening of the nozzle where the source conditions such as temperature, density, and velocity are specified at the nozzle opening and not equal to the stagnation conditions well inside the nozzle reservoir. Nevertheless, the collision rate and mean free path are such that the flow begins well into the continuum regime. The criteria for continuum flow can be described using the Knudsen number Kn, given by

$$\text{Kn} = \frac{\lambda_{\text{mfp}}}{L}, \tag{A1}$$

where $\lambda_{\text{mfp}}$ is the mean free path and $L$ is a characteristic length scale. Generally, the condition for continuum flow is satisfied when Kn $< 0.01$ [66]. The Knudsen numbers for simulations of the helium jet at the opening of the nozzle, where $L$ is the nozzle diameter, are such that Kn $< 0.005$.

The form for $\zeta_{\text{He}}(\hat{r})$ in Eq. (4) that we use is based on findings from measurements in low-density wind tunnels [67] as well as in supersonic molecular jets using linear Raman spectroscopy [68]. The form was observed for $\theta < 20°$ as shock fronts occurred in these experiments. In our model, we assume a sufficiently low background pressure such that the helium smoothly transitions to free molecular flow without the formation of shocks. This is due to the charcoal adsorption pump used in the apparatus to remove background helium atoms. Nevertheless, it is desirable to test this functional form at higher angles.

For a given nozzle shape and opening nozzle diameter, the angular density profile is expected to be independent of the stagnation density and temperature so long as the flow begins in the continuum regime. As such, the helium expansion can be simulated to large angles from the centerline to compare with Eq. (4).

Results comparing the analytic profile to simulations for various nozzle temperatures and densities are shown in Fig. 14. Agreement with Eq. (7) is generally within 6% for angles $\theta$ up to 30° with inaccuracies of up to 30% at larger angles around 55°. We note that running our simulations with other functional forms of $\zeta_{\text{He}}(\hat{r})$ for $\theta > 20°$ results in negligible differences in the seeding efficiency as few AM-$^4$He collisions occur for large angles $\theta$.

Density and speed profiles are presented in Fig. 15 for a sonic nozzle with an opening diameter of 0.2 mm. The flow speed decreases from the expected terminal velocity for
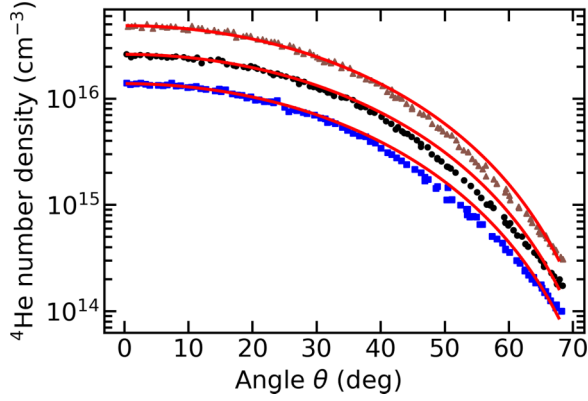
FIG. 14. Angular number density profile of a $^4$He expansion with simulated results (markers) and analytic profile (red curve) as a function of angle $\theta$. Results are for $^4$He densities at the nozzle opening with diameter $d_N = 0.2$ mm and nozzle opening temperatures of $4 \times 10^{19}$ cm$^{-3}$ and 300 K (brown triangles), $2 \times 10^{19}$ cm$^{-3}$ and 100 K (black circles), and $1 \times 10^{19}$ cm$^{-3}$ and 200 K (blue squares).

large angles with the speed dropping by 5% from $\theta = 0$ to $\theta = 70°$. At large angles the collision rate is not sufficient to maintain local thermal equilibrium and the conversion of random thermal motion into forward kinetic energy ceases after a short distance. As our source has a greater collision rate, the variations in flow speed in Fig. 15 are expected to be an upper bound for variations we might expect. Nevertheless, the disagreement with Eq. (3) at large angles is negligible as the AM-$^4$He relative velocities are dominated by the AM velocity at large angles.

In the lithium seeding simulation, the calculation of the helium jet parameters relies on the assumption that our region of interest is within the continuum-flow regime of the jet. To examine the validity of this assumption, we investigated the transition of a helium expansion from the continuum-flow regime to the free-molecular-flow regime using the DS2V software. The ratio $T_\perp/T_\parallel$ of transverse to longitudinal temperature along the centerline of the jet is commonly used as a parameter to quantify the level of thermal equilibrium as the
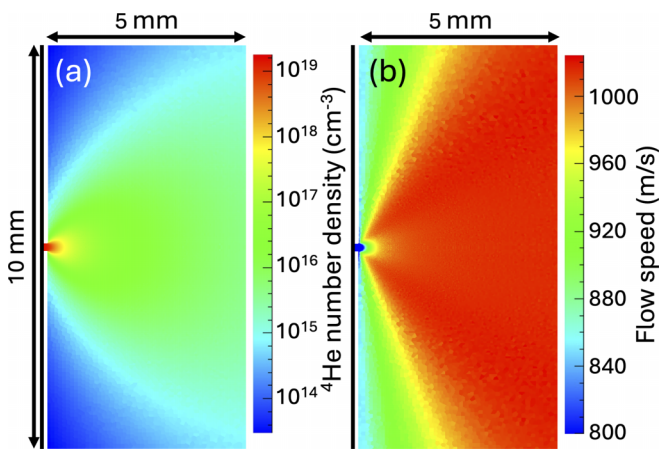


FIG. 15. Simulated (a) $^4$He number density profile and (b) flow speed profile for a helium expansion with a nozzle opening temperature of 100 K and nozzle diameter of 0.2 mm.
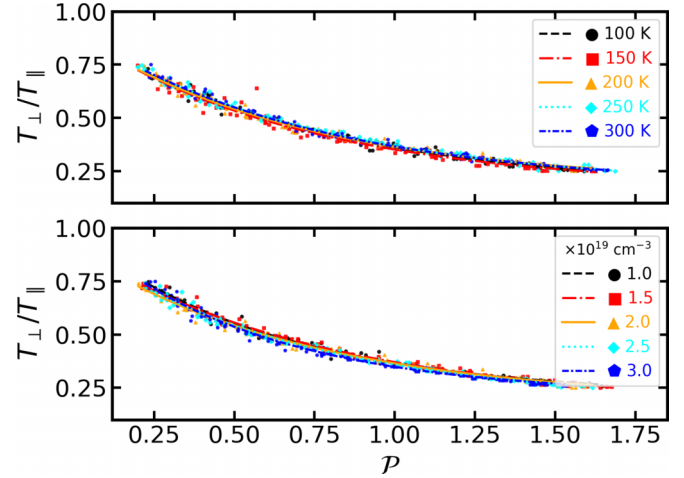


FIG. 16. Temperature ratio plotted as a function of the nonequilibrium parameter $\mathcal{P}$ for various conditions at the opening of the nozzle. DSMC simulated results (markers) are fit to an inverse power law (solid lines). (a) Nozzle opening density fixed at $2 \times 10^{19}$ cm$^{-3}$ with varying starting temperatures. (b) Nozzle opening temperature fixed at 200 K with varying nozzle opening densities.

jet transitions from continuum to free-molecular flow [38,49]. It has been shown [66] that the continuum-flow assumptions are valid if the collision rate $\Gamma$ is much larger than the proportional rate of change of density $n_{He}$ such that

$$\Gamma \gg \frac{1}{n_{He}}\frac{dn_{He}}{dt}. \tag{A2}$$

This motivated [69] the definition of a nonequilibrium parameter $\mathcal{P}$ defined as

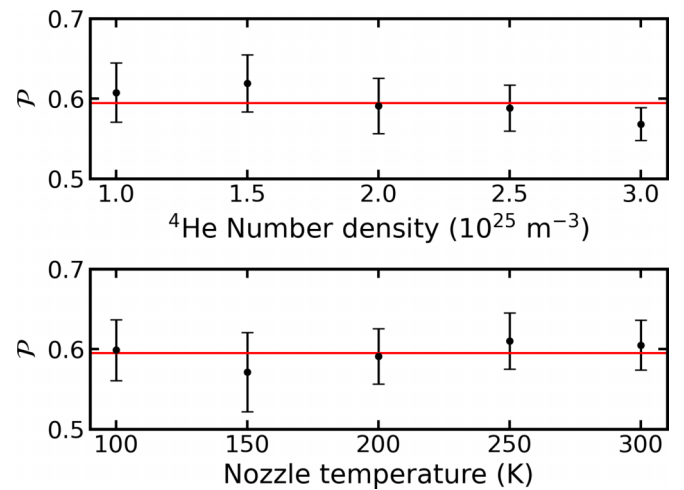$$\mathcal{P} = \frac{1}{\Gamma}\left|\frac{d(\ln n_{He})}{dt}\right|, \tag{A3}$$



FIG. 17. Value of the nonequilibrium parameter $\mathcal{P}$ for $T_\perp/T_\parallel = 0.5$ for various starting conditions in the DSMC simulation. Results are shown for (a) a nozzle opening density of $2 \times 10^{19}$ cm$^{-3}$ with varying nozzle opening temperature and (b) varying nozzle opening densities for a nozzle opening temperature of 200 K. Error bars represent one standard deviation of uncertainty.
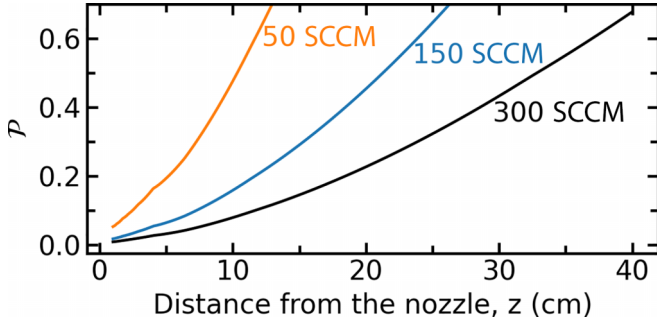
FIG. 18. Parameter $\mathcal{P}$ versus distance from the helium nozzle for various helium flow rates. The parameter $\mathcal{P}$ is calculated assuming an adiabatic expansion of the helium.

which serves as an approximate universal nonequilibrium parameter when investigating the behavior of $T_\perp/T_\parallel$ for various jet conditions [70,71]. As we are interested in near-continuum flow, Eq. (A3) can be expressed as

$$\mathcal{P} = \frac{v_s \lambda_{\mathrm{mfp}}}{\overline{v} n_{\mathrm{He}}} \left| \frac{d n_{\mathrm{He}}}{dr} \right|, \tag{A4}$$

where $v_s$ is the flow speed in the laboratory frame and $\overline{v}$ is the mean velocity in the moving frame. Recognizing from Eq. (7) that

$$\frac{1}{n_{\mathrm{He}}} \left| \frac{d n_{\mathrm{He}}}{dr} \right| = \frac{2}{r}, \tag{A5}$$

$\mathcal{P}$ can now be defined as

$$\mathcal{P} = \frac{2 v_s \lambda_{\mathrm{mfp}}}{\overline{v} r}. \tag{A6}$$

Using the DS2V software, $\mathcal{P}$ is computed using Eq. (A6) for various densities and temperatures at the opening of the nozzle. The transverse and longitudinal velocity distributions, and thus $T_\perp$ and $T_\parallel$, are also computed. Plots of $T_\perp/T_\parallel$ vs $\mathcal{P}$ are shown in Fig. 16. We consider the location where $T_\perp/T_\parallel = 0.5$ as a reasonable estimate for when the probability distribution of the expansion can no longer be well approximated by Eq. (1). This occurs when $\mathcal{P} = 0.60(2)$, as shown in Fig. 17.

From Eqs. (2), (3), and (7), along with the $^4$He-$^4$He cross section from Ref. [46], the parameter $\mathcal{P}$ can be calculated for our source conditions as a function of distance from the helium nozzle. Results for $\mathcal{P}$ along the centerline of the expansion for various helium flow rates are shown in Fig. 18. The values are calculated assuming an adiabatic
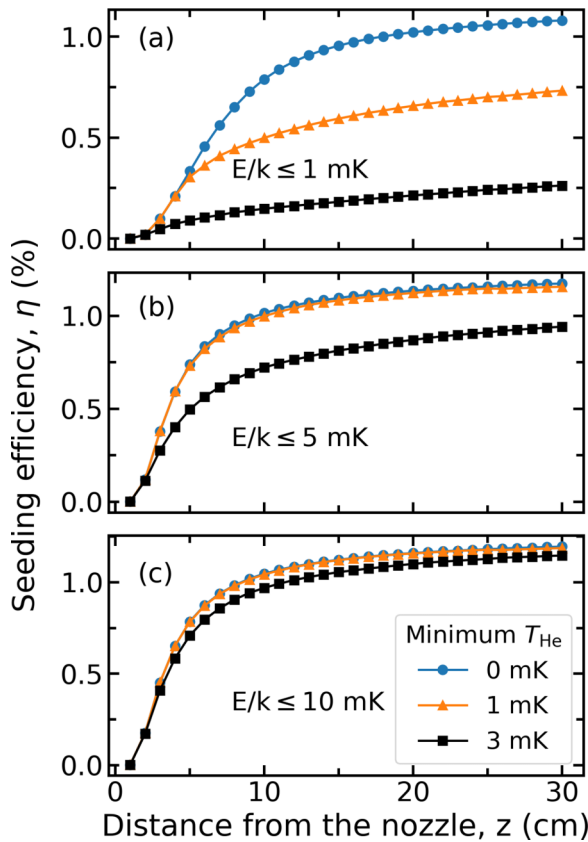


FIG. 19. Seeding efficiency of $^7$Li atoms with energies in the moving frame up to and including (a) $k \times 1$ mK, (b) $k \times 5$ mK, and (c) $k \times 10$ mK versus distance from the nozzle. In each plot, the seeding efficiency is shown for three models of the helium expansion where the minimum helium temperature is set to 0, 1, and 3 mK. The seeding efficiency is specified for a solid angle of 0.02 sr and a helium flow rate of 200 SCCM.



FIG. 20. Seeding efficiency of $^{87}$Rb atoms with energies in the moving frame up to and including (a) $k \times 10$ mK, (b) $k \times 50$ mK, and (c) $k \times 100$ mK versus distance from the nozzle. For each plot, the seeding efficiency is shown for three models of the helium expansion where the minimum helium temperature is set to 0, 1, and 3 mK. The seeding efficiency is specified for a solid angle of 0.02 sr and a helium flow rate of 300 SCCM.
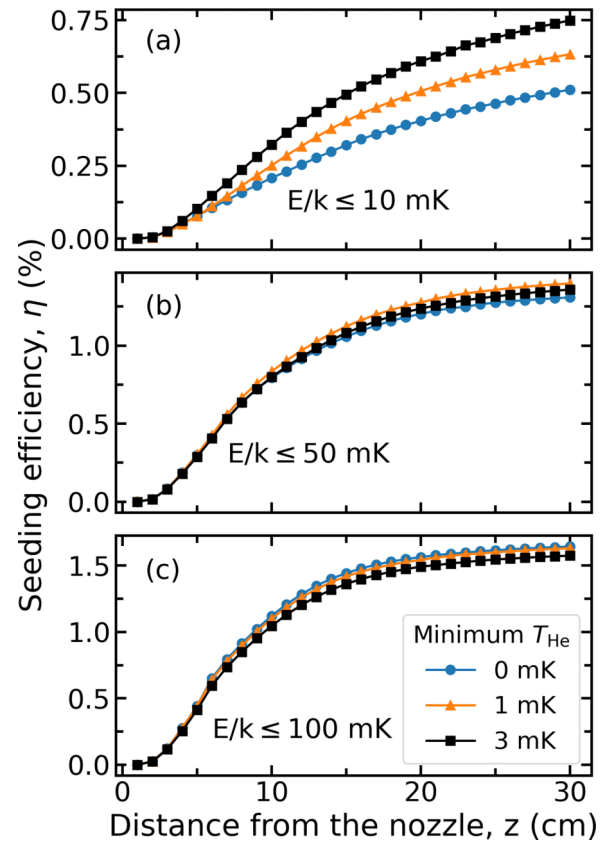
expansion and will become inaccurate as the value of $\mathcal{P}$ becomes large. However, at small to intermediate values of $\mathcal{P}$, the approximate location where the helium collisions begin to turn off can be estimated. Examining the location where $\mathcal{P} = 0.6$, it can be seen that the jet is expected to remain collisional well past the region where seeding occurs. In fact, at the highest flow rate of 300 SCCM, the helium is expected to continue to cool past 20 cm from the nozzle. This would amount to a temperature on the order of 100 µK. It is unlikely, however, that these temperatures will be reached due to cluster formation. At high helium flow rates, cluster formation of the helium can occur, releasing heat of condensation and setting a limit on the cooling. Some of us described in Ref. [12] that at our higher helium flow rates, we are likely in a regime where some cluster formation is occurring. While direct observation of clustering in our jet has not been observed, it has been observed in prior experiments with pure helium expansions. In these experiments, the lowest temperatures that have been achieved are typically around 0.5–1 mK [14,72–74]. As a result, it seems reasonable to conclude that the minimum temperature of the $^4$He jet without the heat load of the alkali-metal atoms is likely comparable to past works.

While cluster formation is not included in the simulation to determine the ultimate limit on the helium temperature, it is still desirable to explore how variations in the helium temperature affect the seeding efficiency. To do this, an artificial temperature floor in the expansion is introduced such that the helium temperature decreases according to Eq. (2) until it reaches a minimum value after which the temperature is constant. This is not a physically accurate way to model heating from cluster formation or decoupling as the jet transitions from continuum to free molecular flow. It does however allow us to explore with a simple model how modifications to the helium velocity distributions affect seeding efficiency. Three different minimum temperatures of 0, 1, and 3 mK are used in the simulations. Results for the seeding efficiency versus distance from the nozzle for these minimum temperatures are shown in Figs. 19 and 20. Here the seeding efficiency is displayed as the percentage of injected alkali-metal atoms within a solid angle of 0.02 sr and with energies up to and including $k \times 1$ mK, $k \times 5$ mK, and $k \times 10$ mK for $^7$Li and $k \times 10$ mK, $k \times 50$ mK, and $k \times 100$ mK for $^{87}$Rb. Unsurprisingly, variations in the helium temperature only have a substantial impact on alkali-metal atoms with low energies in the moving frame. Since this occurs after entrainment, the source conditions that maximize seeding efficiency are unaffected by these variations in the helium temperature. Interestingly, a higher helium temperature results in a high seeding efficiency for $^{87}$Rb at low energies. This is a consequence of the $^4$He-$^{87}$Rb resonance at around 10 mK. Overall, it is likely that the simulation does not accurately predict the final seeding efficiency of $^7$Li atoms with energies less than or equal to $k \times 1$ mK or $^{87}$Rb atoms with energies less than or equal to $k \times 10$ mK. However, it should be reasonably accurate for predicting energies greater than or equal to $k \times 10$ mK and greater than or equal to $k \times 100$ mK for $^7$Li and $^{87}$Rb, respectively.

[1] M. R. Tarbutt, J. J. Hudson, B. E. Sauer, E. A. Hinds, V. A. Ryzhov, V. L. Ryabov, and V. F. Ezhov, A jet beam source of cold YbF radicals, J. Phys. B **35**, 5013 (2002).

[2] P. Aggarwal, H. L. Bethlem, A. Boeschoten, A. Borschevsky, K. Esajas, Y. Hao, S. Hoekstra, K. Jungmann, V. R. Marshall, T. B. Meijknecht, M. C. Mooij, R. G. E. Timmermans, A. Touwen, W. Ubachs, L. Willmann, Y. Yin, and A. Zapara, A supersonic laser ablation beam source with narrow velocity spreads, Rev. Sci. Instrum. **92**, 033202 (2021).

[3] I. Khalil and D. R. Miller, The structure of supercritical fluid free-jet expansions, AIChE J. **50**, 2697 (2004).

[4] N. Suas-David, V. Kulkarni, A. Benidar, S. Kassi, and R. Georges, Line shape in a free-jet hypersonic expansion investigated by cavity ring-down spectroscopy and computational fluid dynamics, Chem. Phys. Lett. **659**, 209 (2016).

[5] R. E. Smalley, L. Wharton, and D. H. Levy, Molecular optical spectroscopy with supersonic beams and jets, Acc. Chem. Res. **10**, 139 (1977).

[6] M. A. Duncan, Invited review article: Laser vaporization cluster sources, Rev. Sci. Instrum. **83**, 041101 (2012).

[7] N. Daugey, P. Caubet, B. Retail, M. Costes, A. Bergeat, and G. Dorthe, Kinetic measurements on methylidyne radical reactions with several hydrocarbons at low temperatures, Phys. Chem. Chem. Phys. **7**, 2921 (2005).

[8] B. Yan, P. F. H. Claus, B. G. M. van Oorschot, L. Gerritsen, A. T. J. B. Eppink, S. Y. T. van de Meerakker, and D. H. Parker, A new high intensity and short-pulse molecular beam valve, Rev. Sci. Instrum. **84**, 023102 (2013).

[9] M. Hillenkamp, S. Keinan, and U. Even, Condensation limited cooling in supersonic expansions, J. Chem. Phys. **118**, 8699 (2003).

[10] K. S. Melin, P. I. Nagornykh, Y. Lu, L. E. Hillberry, Y. Xu, and M. G. Raizen, Observation of a quasi-one-dimensional variation of the Stern-Gerlach effect, Phys. Rev. A **99**, 063417 (2019).

[11] F. M. H. Crompvoets, R. T. Jongma, H. L. Bethlem, A. J. A. van Roij, and G. Meijer, Longitudinal focusing and cooling of a molecular beam, Phys. Rev. Lett. **89**, 093004 (2002).

[12] W. Huntington, J. Glick, M. Borysow, and D. J. Heinzen, Intense continuous cold-atom source, Phys. Rev. A **107**, 013302 (2023).

[13] O. F. Hagena, Condensation in free jets: Comparison of rare gases and metals, Z. Phys. D **4**, 291 (1987).

[14] J. Wang, V. A. Shamamian, B. R. Thomas, J. M. Wilkinson, J. Riley, C. F. Giese, and W. R. Gentry, Speed ratios greater than 1000 and temperatures less than 1 mK in a pulsed He beam, Phys. Rev. Lett. **60**, 696 (1988).

[15] S. DePaul, D. Pullman, and B. Friedrich, A pocket model of seeded supersonic beams, J. Phys. Chem. **97**, 2167 (1993).

[16] O. Schullian, J. Loreau, N. Vaeck, A. van der Avoird, B. Heazlewood, C. Rennick, and T. Softley, Simulating rotationally inelastic collisions using a direct simulation Monte Carlo method, Mol. Phys. **113**, 3972 (2015).

[17] N. Abuaf, J. B. Anderson, R. P. Andres, J. B. Fenn, and D. G. H. Marsden, Molecular beams with energies above one electron volt, Science **155**, 997 (1967).

[18] G. B. Ury and L. Wharton, Absolute total scattering cross sections of $^7$Li–Ar, J. Chem. Phys. **56**, 5832 (1972).

[19] P. Dehmer and L. Wharton, Absolute total scattering cross sections for $^7$Li on He, Ne, Kr, and Xe, J. Chem. Phys. **57**, 4821 (1972).

[20] T. R. Marrero and E. A. Mason, Gaseous diffusion coefficients, J. Phys. Chem. Ref. Data **1**, 3 (1972).

[21] W. A. Hamel, J. E. M. Haverkort, H. G. C. Werij, and J. P. Woerdman, Calculation of alkali-noble gas diffusion cross sections relevant to light-induced drift, J. Phys. B **19**, 4127 (1986).

[22] A. A. Medvedev, V. V. Meshkov, A. V. Stolyarov, and M. C. Heaven, *Ab initio* interatomic potentials and transport properties of alkali metal (M = Rb and Cs)–rare gas (Rg = He, Ne, Ar, Kr, and Xe) media, Phys. Chem. Chem. Phys. **20**, 25974 (2018).

[23] A. Pouliot, G. Carlse, H. C. Beica, T. Vacheresse, A. Kumarakrishnan, U. Shim, S. B. Cahn, A. Turlapov, and T. Sleator, Accurate determination of an alkali-vapor–inert-gas diffusion coefficient using coherent transient emission from a density grating, Phys. Rev. A **103**, 023112 (2021).

[24] H. Partridge, J. R. Stallcop, and E. Levin, Potential energy curves and transport properties for the interaction of He with other ground-state atoms, J. Chem. Phys. **115**, 6471 (2001).

[25] R. Brühl and D. Zimmermann, High-resolution laser spectroscopy of LiAr: Improved interaction potential and spin-rotation-coupling in the ground state X $^2\Sigma^+$, J. Chem. Phys. **115**, 7892 (2001).

[26] I. S. K. Kerkines and A. Mavridis, Theoretical investigation of the X $^2\Sigma^+$, A $^2\Pi$, and B $^2\Sigma^+$ states of LiAr and LiKr, J. Chem. Phys. **116**, 9305 (2002).

[27] U. Kleinekathöfer, M. Lewerenz, and M. Mladenović, Long range binding in alkali-helium pairs, Phys. Rev. Lett. **83**, 4717 (1999).

[28] N. Tariq, N. A. Taisan, V. Singh, and J. D. Weinstein, Spectroscopic detection of the LiHe molecule, Phys. Rev. Lett. **110**, 153201 (2013).

[29] D. E. Fagnan, J. Wang, C. Zhu, P. Djuricanin, B. G. Klappauf, J. L. Booth, and K. W. Madison, Observation of quantum diffractive collisions using shallow atomic traps, Phys. Rev. A **80**, 022712 (2009).

[30] J.-P. Yuan, Z.-H. Ji, Y.-T. Zhao, X.-F. Chang, L.-T. Xiao, and S.-T. Jia, Simple, reliable, and nondestructive method for the measurement of vacuum pressure without specialized equipment, Appl. Opt. **52**, 6195 (2013).

[31] V. B. Makhalov, K. A. Martiyanov, and A. V. Turlapov, Primary vacuometer based on an ultracold gas in a shallow optical dipole trap, Metrologia **53**, 1287 (2016).

[32] P. Shen, K. W. Madison, and J. L. Booth, Realization of a universal quantum pressure standard, Metrologia **57**, 025015 (2020).

[33] P. Shen, K. W. Madison, and J. L. Booth, Refining the cold atom pressure standard, Metrologia **58**, 022101 (2021).

[34] L. H. Ehinger, B. P. Acharya, D. S. Barker, J. A. Fedchak, J. Scherschligt, E. Tiesinga, and S. Eckel, Comparison of two multiplexed portable cold-atom vacuum standards, AVS Quantum Sci. **4**, 034403 (2022).

[35] D. S. Barker, B. P. Acharya, J. A. Fedchak, N. N. Klimov, E. B. Norrgard, J. Scherschligt, E. Tiesinga, and S. P. Eckel, Precise quantum measurement of vacuum with cold atoms, Rev. Sci. Instrum. **93**, 121101 (2022).

[36] J. Kłos and E. Tiesinga, Elastic and glancing-angle rate coefficients for heating of ultracold Li and Rb atoms by collisions with room-temperature noble gases, $H_2$, and $N_2$, J. Chem. Phys **158**, 014308 (2023).

[37] D. S. Barker, J. A. Fedchak, J. Kłos, J. Scherschligt, A. A. Sheikh, E. Tiesinga, and S. P. Eckel, Accurate measurement of the loss rate of cold atoms due to background gas collisions for the quantum-based cold atom vacuum standard, AVS Quantum Sci. **5**, 035001 (2023).

[38] J. P. Toennies and K. Winkelmann, Theoretical studies of highly expanded free jets: Influence of quantum effects and a realistic intermolecular potential, J. Chem. Phys. **66**, 3965 (1977).

[39] R. H. Edwards and H. K. Cheng, Steady expansion of a gas into a vacuum, AIAA J. **4**, 558 (1966).

[40] B. B. Hamel and D. R. Willis, Kinetic theory of source flow expansion with application to the free jet, Phys. Fluids **9**, 829 (1966).

[41] S. A. E. Miller, J. Veltin, P. J. Morris, and D. K. McLaughlin, Assessment of computational fluid dynamics for supersonic shock containing jets, AIAA J. **47**, 2738 (2009).

[42] J. A. Wilkes, C. E. Glass, P. M. Danehy, and R. J. Nowak, Fluorescence imaging of underexpanded jets and comparison with CFD, in *Proceedings of the 44th AIAA Aerospace Sciences Meeting and Exhibit, Reno, 2006* (AIAA, Reston, VA, 2006), paper AIAA 2006-910.

[43] M. Usami and K. Teshima, Molecular simulation of rarefied supersonic free jets by DSMC method, JSME Int. J. Ser. B **42**, 369 (1999).

[44] U. Even, The Even-Lavie valve as a source for high intensity supersonic beam, EPJ Tech. Instrum. **2**, 17 (2015).

[45] O. Schullian, H. S. Antila, and B. R. Heazlewood, A variable time step self-consistent mean field DSMC model for three-dimensional environments, J. Chem. Phys. **156**, 124309 (2022).

[46] M. Chrysos, Dirac bubble potential for He–He and inadequacies in the continuum: Comparing an analytic model with elastic collision experiments, J. Chem. Phys. **146**, 024106 (2017).

[47] H. Pauly, *Atom, Molecule, and Cluster Beams I* (Springer, Berlin, 2000).

[48] D. R. Miller, in *Atomic and Molecular Beam Methods*, edited by G. Scoles (Oxford University Press, Oxford, 1988), Vol. 1, pp. 14–53.

[49] H. Beijerinck and N. Verster, Absolute intensities and perpendicular temperatures of supersonic beams of polyatomic gases, Physica B+C **111**, 327 (1981).

[50] J. R. Taylor, *Scattering Theory* (Dover, Mineola, 1972).

[51] M. S. Child, *Molecular Collision Theory* (Academic, New York, 1974).

[52] A. Messiah, *Quantum Mechanics*, 2nd ed. (Dunod, Paris, 1995).

[53] C. Makrides, D. S. Barker, J. A. Fedchak, J. Scherschligt, S. Eckel, and E. Tiesinga, Collisions of room-temperature helium with ultracold lithium and the van der Waals bound state of HeLi, Phys. Rev. A **101**, 012702 (2020).

[54] C. Makrides, D. S. Barker, J. A. Fedchak, J. Scherschligt, S. Eckel, and E. Tiesinga, Erratum: Collisions of room-temperature helium with ultracold lithium and the van der Waals bound state of HeLi, [Phys. Rev. A **101**, 012702 (2020)], Phys. Rev. A **105**, 029902(E) (2022).

[55] A. Derevianko, S. G. Porsev, and J. F. Babb, Electric dipole polarizabilities at imaginary frequencies for hydrogen, the

alkali–metal, alkaline–earth, and noble gas atoms, At. Data Nucl. Data Tables **96**, 323 (2010).

[56] P. T. Greenland, M. A. Lauder, and D. J. H. Wort, Atomic beam velocity distributions, J. Phys. D **18**, 1223 (1985).

[57] P. K. Romano and J. A. Walsh, An improved target velocity sampling algorithm for free gas elastic scattering, Ann. Nucl. Energy **114**, 318 (2018).

[58] S. K. Lam, A. Pitrou, and S. Seibert, in *Proceedings of the Second Workshop on the LLVM Compiler Infrastructure in HPC* (Association for Computing Machinery, New York, 2015).

[59] D. Das and V. Natarajan, Absolute frequency measurement of the lithium *D* lines: Precise determination of isotope shifts and fine-structure intervals, Phys. Rev. A **75**, 052508 (2007).

[60] A. Kramida, Y. Ralchenko, J. Reader, and NIST ASD Team, NIST Atomic Spectra Database, available at https://physics.nist.gov/asd (National Institute of Standards and Technology, Gaithersburg, 2023), version 5.11.

[61] N. R. Hutzler, H.-I. Lu, and J. M. Doyle, The buffer gas beam: An intense, cold, and slow source for atoms and molecules, Chem. Rev. **112**, 4803 (2012).

[62] H. L. Bethlem, G. Berden, and G. Meijer, Decelerating neutral dipolar molecules, Phys. Rev. Lett. **83**, 1558 (1999).

[63] K. Luria, W. Christen, and U. Even, Generation and propagation of intense supersonic beams, J. Phys. Chem. A **115**, 7362 (2011).

[64] M. J. Doppelbauer, O. Schullian, J. Loreau, N. Vaeck, A. van der Avoird, C. J. Rennick, T. P. Softley, and B. R. Heazlewood,

Using a direct simulation Monte Carlo approach to model collisions in a buffer gas cell, J. Chem. Phys. **146**, 044302 (2017).

[65] G. Bird, http://www.gab.com.au/.

[66] G. A. Bird, *Molecular Gas Dynamics and the Direct Simulation of Gas Flows*, Oxford Engineering Science Series Vol. 42 (Clarendon, Oxford, 1994).

[67] H. Ashkenas and F. S. Sherman, The structure and utilization of supersonic free jets in low density wind tunnels, in *Rarefied Gas Dynamics*, *Rarefied Gas Dynamics, Volume 2*, edited by J. H. de Leeuw (Academic, New York, 1965), Vol. 2, p. 84.

[68] G. Tejeda, B. Maté, J. M. Fernández-Sánchez, and S. Montero, Temperature and density mapping of supersonic jet expansions using linear Raman spectroscopy, Phys. Rev. Lett. **76**, 34 (1996).

[69] G. A. Bird, Breakdown of translational and rotational equilibrium in gaseous expansions, AIAA J. **8**, 1998 (1970).

[70] A. E. Zarvin and R. G. Sharafutdinov, Rotational relaxation in the transition regime of free nitrogen jets, J. Appl. Mech. Tech. Phys. **22**, 737 (1982).

[71] I. D. Boyd, G. Chen, and G. V. Candler, Predicting failure of the continuum fluid equations in transitional hypersonic flows, Phys. Fluids **7**, 210 (1995).

[72] F. Luo, G. C. McBane, G. Kim, C. F. Giese, and W. R. Gentry, The weakest bond: Experimental observation of helium dimer, J. Chem. Phys. **98**, 3564 (1993).

[73] L. W. Bruch, W. Schöllkopf, and J. P. Toennies, The formation of dimers and trimers in free jet $^4$He cryogenic expansions, J. Chem. Phys. **117**, 1544 (2002).

[74] L. Pedemonte and G. Bracco, Study of He flow properties to test He dimer potentials, J. Chem. Phys. **119**, 1433 (2003).